



**Development of a Time-Dependent
View Factor Code for Studying
Radiation Symmetry in ICF Hohlräume**

J.J. MacFarlane

February 1998

UWFDM-1061

FUSION TECHNOLOGY INSTITUTE

UNIVERSITY OF WISCONSIN

MADISON WISCONSIN

DISCLAIMER

This report was prepared as an account of work sponsored by an agency of the United States Government. Neither the United States Government, nor any agency thereof, nor any of their employees, makes any warranty, express or implied, or assumes any legal liability or responsibility for the accuracy, completeness, or usefulness of any information, apparatus, product, or process disclosed, or represents that its use would not infringe privately owned rights. Reference herein to any specific commercial product, process, or service by trade name, trademark, manufacturer, or otherwise, does not necessarily constitute or imply its endorsement, recommendation, or favoring by the United States Government or any agency thereof. The views and opinions of authors expressed herein do not necessarily state or reflect those of the United States Government or any agency thereof.

**Development of a Time-Dependent View Factor Code
for Studying Radiation Symmetry in ICF Hohlräume**

Joseph J. MacFarlane

Fusion Technology Institute
University of Wisconsin-Madison
1500 Engineering Drive
Madison, WI 53706

February 1998

UWFDM-1061

Contents

1. Introduction	1
2. Grid Generation	3
3. Evaluation of Configuration Factor Integrals	6
3.1. Evaluation of Individual Segment-to-Segment Combinations	7
4. Self-Occultation Effects	13
5. Blocking By Intervening Surfaces	16
6. Solution of the Radiosity Equation	19
7. Laser Deposition Ray-Trace Algorithm	20
8. Graphics	25
9. Benchmark Calculations	26
9.1. Evaluation of Different Configuration Factor Integration Methods	26
9.2. Concentric Sphere Benchmark Calculations	27
9.3. Summary of Benchmark Simulations	43
10. Simulations of NOVA and OMEGA Radiation Symmetry Experiments	44
10.1. Simulation of NOVA Radiation Symmetry Experiments	44
10.2. Simulation of OMEGA Tetrahedral Hohlraums	46

1. Introduction

The purpose of this report is to summarize work performed at the University of Wisconsin for Los Alamos National Laboratories during the period from Oct. 1, 1996 through Sept. 30, 1997. The primary objective of this work has been to develop a time-dependent 3-D view factor code for the purpose of simulating asymmetric radiation fields incident onto a capsule in indirect-drive inertial confinement fusion (ICF) experiments. The capabilities of the code include: utilizing time-dependent albedos for the hohlraum wall based on 1-D radiation-hydrodynamics simulations [1] and multifrequency UTA (unresolved transition array) opacities [2,3]; and modeling the time-dependent laser powers of the NOVA, OMEGA, and NIF beams. Examples of experiments for which the code will be applied include: radiation symmetry studies for tetrahedral hohlraums, beam phasing, and azimuthal asymmetries in cylindrical hohlraums. The statement of work for the first year of this effort is shown in Table 1.1.

In developing the view factor code, we have chosen to focus on accuracy. Radiosity (i.e., view factor) methods have been developed in the field of computer graphics [4-9] which emphasize speed, but at a cost of reduced accuracy. Since we are in particular interested in computing asymmetries on an ICF capsule with numerical errors of less than 1%, we have developed and benchmarked methods for evaluating configuration factors (or view factors) with a high degree of accuracy.

The view factor code we have developed is called SYMRAD. In this report, we will describe the attributes of the following models and algorithms in the code:

- Grid generation
- Evaluation of configuration factor integrals
- Self-occultation (or “horizon effects”)
- Occultation by other objects/surfaces
- Solution to the radiosity equation
- Laser deposition ray-trace algorithm
- Graphics

Each of the above items is described individually in Sections 2 through 8. In Section 9 we describe several idealized benchmark calculations to test the accuracy of the code. Finally, in Section 10 initial calculations relevant to ICF radiation symmetry experiments utilizing cylindrical and tetrahedral hohlraums are presented.

Table 1.1. Tasks for October 1996–September 1997

Develop a three-dimensional computer code that uses vacuum transport between surfaces to model the flow of radiation inside a hohlraum. The code will calculate the view factors between all of the surfaces. One-dimensional radiation-hydrodynamics simulations with U. Wisconsin opacities calculated with the UTA method will be used to calculate the emissivities and albedos of all surfaces. The code will model the radiation flow in a time-dependent manner, where the emissivities and albedos are calculated as functions of time. An arbitrary source term for all surfaces will be included.

1. Develop and document a 3-D radiation transport code in vacuum which incorporates:
 - a. Time-dependent albedos for all surfaces;
 - b. Energy sourcing as a function of time on all surfaces;
 - c. An input form that conveniently allows users to construct surfaces, sources, and initial conditions;
 - d. Output of the time-dependent radiant flux on user-defined surfaces.
2. Demonstrate code performance at U. Wisconsin by calculating test problems mutually agreed to by UW and LANL scientists.
3. Deliver and assist in the installation of the 3-D code at LANL.

2. Grid Generation

At present, the SYMRAD code can generate grids for the following “objects”:

- spheres
- cylinders
- disks (or annular rings)
- planes
- tetrahedral spheres
(i.e., spheres with 4 circular openings at the apexes of a tetrahedron)

Each object is divided into a number of planar surface elements. These surfaces are either triangles or quadrilaterals. The user specifies, through namelist input files, the type of object and the grid resolution. Obviously, greater accuracy is usually achieved by using a finer mesh with a larger number of surfaces. To date, calculations have been performed with up to 1200 surfaces on an HP workstation with 80 MB of RAM. The CPU time required for a stand-alone calculation (i.e., without utilizing the radiation-hydrodynamics option) is approximately 15 CPU minutes on a HP 735 workstation.

Using the above objects, it is possible to investigate the symmetry of the incident radiation field on capsules in both cylindrical hohlraums with 2 laser entrance holes (LEH) and tetrahedral hohlraums with 4 LEH. Figures 2.1 and 2.2 show sample grids for cylindrical and tetrahedral hohlraums, respectively.

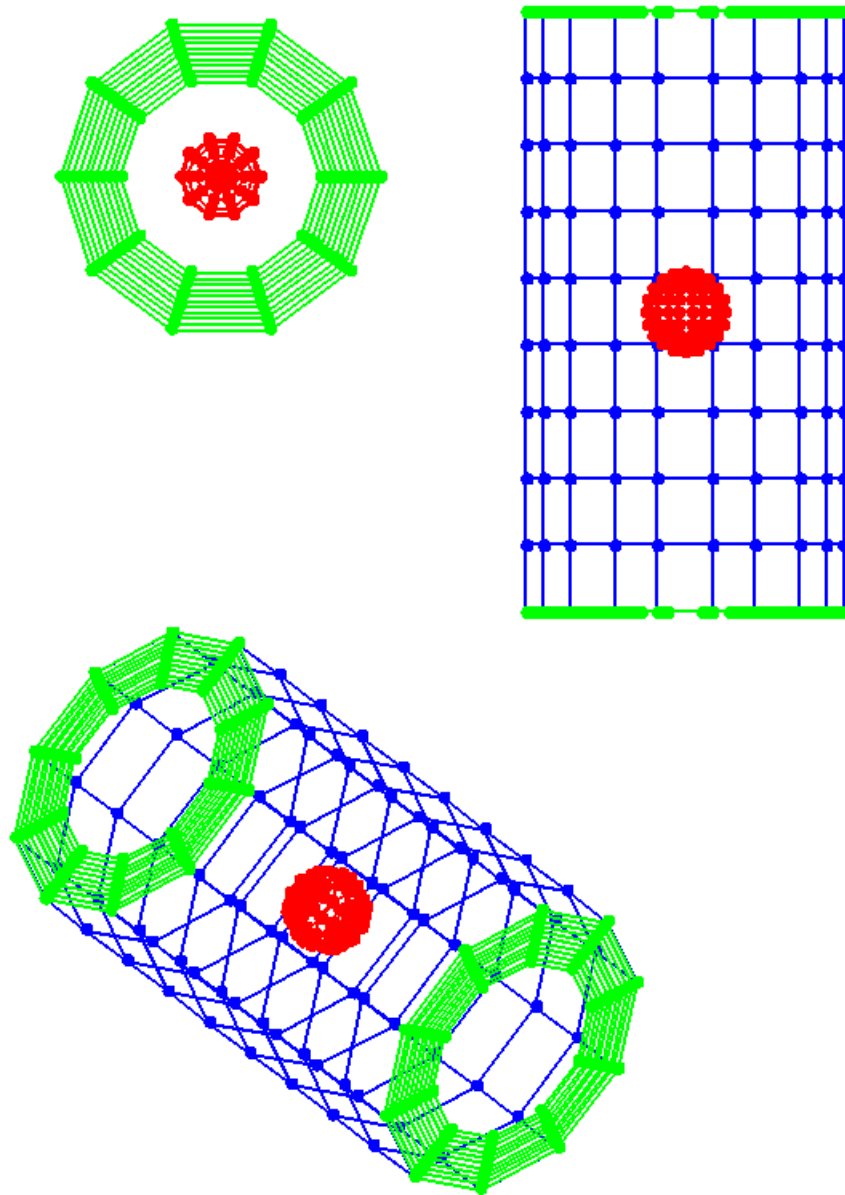


Figure 2.1. Grid generated for a cylindrical hohlraum. Top left: view through LEH. Top right: view from side. Lower left: off-axis view. A spherical capsule (red) is located at the center of the hohlraum.

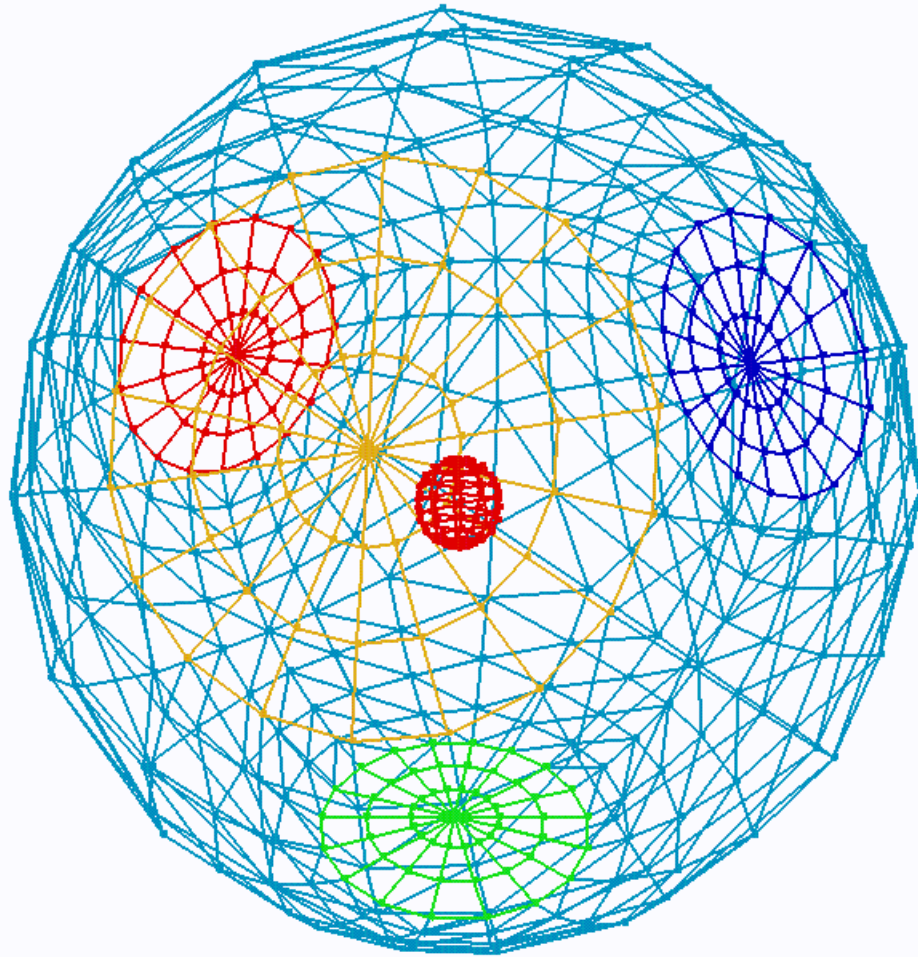


Figure 2.2. Grid generated for tetrahedral hohlraum. The 4 LEH are shown in red, green, yellow, and dark blue. The capsule is the small sphere at the center.

3. Evaluation of Configuration Factor Integrals

The configuration factor, or view factor, for two finite areas can be written as [10]:

$$F_{ij} = \frac{1}{2\pi A_i} \int_{A_i} \int_{A_j} \frac{\cos \theta_i \cos \theta_j}{\pi S^2} dA_i dA_j \quad (3.1)$$

where A_i and A_j are the areas of surfaces i and j , respectively, S is the distance between differential elements dA_i and dA_j , and θ_i (θ_j) is the angle between the surface normal vector of element dA_i (dA_j). Physically, F_{ij} is the fraction of energy leaving surface i that arrives at surface j . Equation (2.1) assumes Lambertian (or diffuse) surfaces, so that the angular dependence of the emissive power is proportional to $\cos \theta$ (as does a blackbody surface).

The reciprocity relation for configuration factors is:

$$A_i F_{ij} = A_j F_{ji} . \quad (3.2)$$

In our view factor code, we take advantage of the reciprocity relation by computing view factors as follows:

- F_{ij} ($i < j$) are evaluated numerically
- F_{ij} ($i = j$) = 0
- F_{ij} ($i > j$) = $(A_j/A_i)F_{ji}$.

In this section, we describe four methods for evaluating Eq. (3.1). Each of these is contained in SYMRAD. These methods have been benchmarked against each other and known analytic solutions to assess trade-offs in accuracy and computational efficiency. These benchmark calculations are described in Section 9. For three of these methods, we apply Stokes' theorem [10] to replace the quadruple integral (two areal integrals) in Eq. (3.1) with a double contour integral, which can be written as:

$$F_{ij} = \frac{1}{2\pi A_i} \oint_{C_i} \oint_{C_j} (\ln S \, dx_j dx_i + \ln S \, dy_j dy_i + \ln S \, dz_j dz_i) . \quad (3.3)$$

Thus, the integral over two areas is replaced by integrals over the boundaries about the two surfaces (see Figure 3.1). This allows for a considerable savings in computer time [4].

In the illustration shown in Figure 3.1, the double contour integral represents the sum of 16 segment-to-segment combinations (the boundary of each quadrilateral

is composed for 4 segments.) Thus, to evaluate configuration factors for the many triangular and quadrilateral surface elements which make up the hohlraum and capsule in our simulation, we desire an accurate, but efficient method for computing each of the segment-to-segment combinations contained in Eq. (3.3).

3.1. Evaluation of Individual Segment-to-Segment Combinations

Let us define:

$$\gamma_{\alpha\beta} = \int_{A_\alpha}^{B_\alpha} \int_{A_\beta}^{B_\beta} \ln S (dx_\alpha dx_\beta + dy_\alpha dy_\beta + dz_\alpha dz_\beta) , \quad (3.4)$$

where A_α and B_α define the end points of segment σ_α which has length L_α , and A_β and B_β define the end points of segment σ_β which has length L_β . In Eq. (3.4), the distance between points on the segments, S , varies as we move along each segment. Note that the total configuration factor is:

$$F_{ij} = \frac{1}{2\pi A_i} \sum_\alpha \sum_\beta \gamma_{\alpha\beta} . \quad (3.5)$$

We next do a coordinate transformation to locate one of the segments along the z-axis and place one of its end points at the origin (see Figure 3.2(b)). Then Eq. (3.4) becomes:

$$\gamma_{\alpha\beta} = \int_0^{L_\alpha} dz_\alpha \int_{Z_\beta^0}^{Z_\beta^1} dz_\beta \ln S . \quad (3.6)$$

Note that the first two terms of Eq. (3.4) can be dropped because segment σ_α is parallel to the z-axis. We write the integrand as:

$$\ln S = \frac{1}{2} \ln[x_\beta^2 + y_\beta^2 + (z_\beta - z_\alpha)^2] . \quad (3.7)$$

Next, we define $t_\alpha = z_\alpha/L_\alpha$ and $t_\beta = (z_\beta - z_{\beta 0})/\Delta z_\beta$, where $\Delta z_\beta = z_{\beta 1} - z_{\beta 0}$ (see Figure 3.2). We then have:

$$\gamma_{\alpha\beta} = \frac{L_\alpha \Delta z_\beta}{2} \int_0^1 dt_\beta \int_0^1 dt_\alpha \ln[S(t_\alpha, t_\beta)^2] . \quad (3.8)$$

Note that t_α and t_β represent the fractional distance moved along segments α and β , respectively. At this point, $\gamma_{\alpha\beta}$ can be evaluated numerically by performing the double integration:

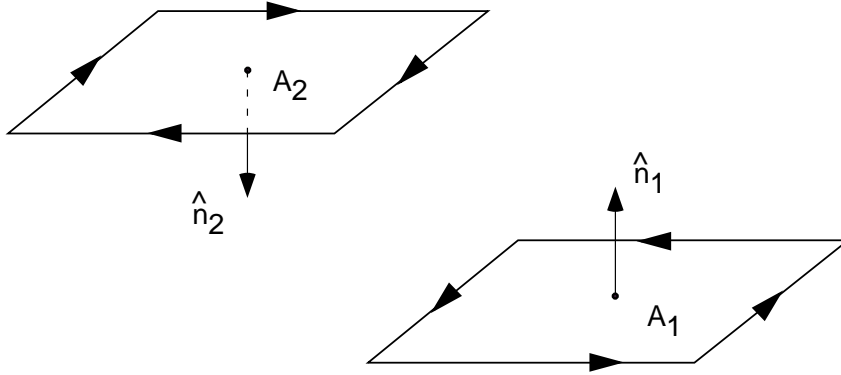


Figure 3.1. Two surface elements illustrating contour integration technique.

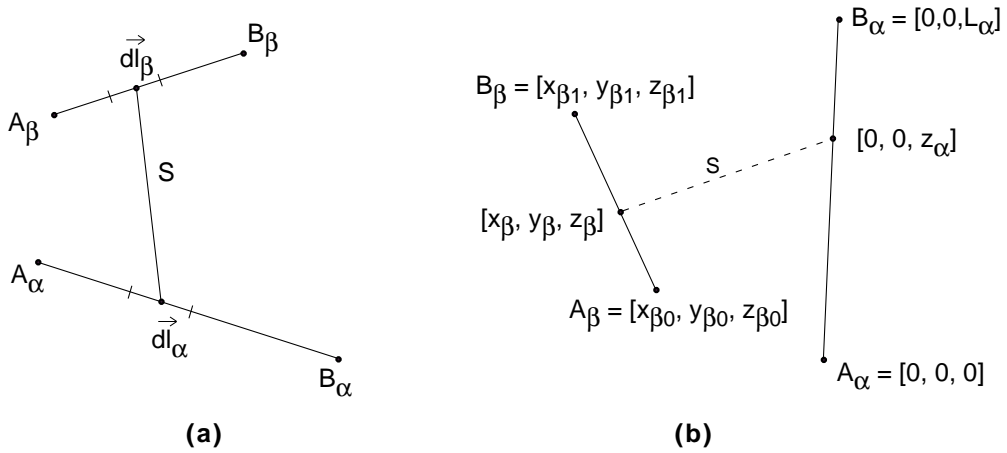


Figure 3.2. Illustrations showing segment-to-segment couplings for contour integration solution of configuration factor integrals. (a) Original coordinate system. (b) Same segments in transformed coordinate system.

$$\gamma_{\alpha\beta} = \frac{L_\alpha \Delta z_\beta}{2} \sum_k^{N_\alpha} w_k \sum_j^{N_\beta} w_j \ln[S(t_j, t_k)^2], \quad (3.9)$$

where w_k and w_j are integration weights. This method, which is often used in view factor codes [4,9], is easily performed by breaking segments α and β into N_α and N_β sub-segments. This evaluation technique will be referred to as Method 1 in our discussion of configuration factor benchmark calculations (see Section 9).

Significant additional accuracy – as well as computational efficiency in some cases – can be obtained by performing an analytic integration of the inside integral in Eq. (3.8). To do this, we define:

$$I_1(t_\beta) = \int_0^1 dt_\alpha \ln[S(t_\alpha, t_\beta)^2]. \quad (3.10)$$

Noting that:

$$S^2 = x_\beta^2 + y_\beta^2 + (z_\beta - z_\alpha)^2 = a + b t_\alpha + c t_\alpha^2, \quad (3.11)$$

where:

$$\begin{aligned} a &= [x_\beta(t_\beta)]^2 + [y_\beta(t_\beta)]^2 + [z_\beta(t_\beta)]^2 \\ b &= -2L_\alpha z_\beta(t_\beta) \\ c &= L_\alpha^2, \end{aligned}$$

and

$$\begin{aligned} x_\beta &= x_{\beta 0} + t_\beta \Delta x_\beta; & \Delta x_\beta &= x_{\beta 1} - x_{\beta 0} \\ y_\beta &= y_{\beta 0} + t_\beta \Delta y_\beta; & \Delta y_\beta &= y_{\beta 1} - y_{\beta 0} \\ z_\beta &= z_{\beta 0} + t_\beta \Delta z_\beta; & \Delta z_\beta &= z_{\beta 1} - z_{\beta 0}, \end{aligned}$$

we have:

$$\begin{aligned} I_1(t_\beta) &= \left(1 + \frac{b}{2c}\right) \ln[a + b + c] - \frac{b}{2c} \ln[a] - 2 \\ &\quad + \frac{q}{c} \left[\tan^{-1} \left(\frac{2c + b}{q} \right) - \tan^{-1} \left(\frac{b}{q} \right) \right] \end{aligned} \quad (3.12)$$

where a and b , as indicated above, are functions of t_β , and $q = (4ac - b^2)^{\frac{1}{2}}$.

[The above solution is valid for cases when $(4ac - b^2) = (x_\beta^2 + y_\beta^2) > 0$; that is, when the points of segment β are not on the segment α axis — such as in the case of co-aligned segments, or identical segments. The latter cases are readily treated analytically.]

Eq. (3.8) then becomes:

$$\gamma_{\alpha\beta} = \frac{L_\alpha \Delta z_\beta}{2} \sum_k^{N_\beta} w_k I_1(t_k) . \quad (3.13)$$

This evaluation technique will be referred to as Method 2 in Section 9. Solutions using this technique can be significantly more accurate than using Eq. (3.9) because the inner integral is evaluated analytically. In addition, it often requires less computer time because only segment β is broken up into subsegments. (For example, if $N_\alpha = N_\beta = 10$, $\ln[S^2]$ in Eq. (3.9) must be evaluated 100 times, whereas $I_1(t_\beta)$ must be evaluated only 10 times in Eq. (3.13).)

Additional accuracy can be achieved in most cases by evaluating the remaining integral analytically for the first three terms of $I(t_\beta)$ in Eq. (3.12). Integrating over the first three terms in Eq. (3.12), and reorganizing the last two (\tan^{-1}) terms, we obtain:

$$\gamma_{\alpha\beta} = \frac{L_\alpha \Delta z_\beta}{2} I_2 + \Delta z_\beta \int_0^1 dt_\beta r_\beta (\sigma + \theta) \quad (3.14)$$

where

$$\begin{aligned} I_2 = & -2 - 2\rho + \eta(1 - 2h) \\ & + \ln(\Omega L_\beta^2 + (1 + 2h)L_\beta^2) [\rho(1 + h) - \eta(1 + \Omega - 2h^2)] \\ & + \ln(\Omega L_\beta^2) [\rho h - \eta(1 + \Omega - 2h^2)] \\ & + \epsilon(\rho + 2\eta h) \left[\tan^{-1}\left(\frac{2(1+h)}{\epsilon}\right) - \tan^{-1}\left(\frac{2h}{\epsilon}\right) \right] , \end{aligned}$$

and

$$\begin{aligned} \rho &= 1 - (z_\beta/L_\alpha) \\ \eta &= \Delta z_\beta/2L_\alpha \\ h &= \frac{1}{L_\beta} [x_{\beta 0} \Delta x_\beta + y_{\beta 0} \Delta y_\beta + (z_{\beta 0} - 2L_\alpha) \Delta z_\beta] \\ \Omega &= \frac{1}{L_\beta^2} [x_{\beta 0}^2 + y_{\beta 0}^2 + (z_{\beta 0} - L_\alpha)^2] \\ \epsilon &= 2(\Omega - h^2)^{\frac{1}{2}} \\ \theta &= \tan^{-1}(z_\beta/r_\beta) \end{aligned}$$

$$\sigma = \tan^{-1}((L_\alpha - z_\beta)/r_\beta)$$

$$z_\beta = z_{\beta 0} + t_\beta(z_{\beta 1} - z_{\beta 0})$$

and

$$r_\beta = [(x_{\beta 0} + t_\beta \Delta x_\beta)^2 + (y_{\beta 0} + t_\beta \Delta y_\beta)^2]^{\frac{1}{2}} .$$

Evaluation of configuration factors using Eq. (3.14) will be referred to as Method 3 in Section 9. It was found that in most test problems that this method provided both the best accuracy and least CPU solution times. Using this method in our concentric sphere benchmark calculations, we found the errors in computing the configuration factors were much less than the errors introduced by representing the sphere by a finite number of polygons (see Section 9). In SYMRAD, this solution method is used by default, while the use of other methods remains optional.

Finally, a fourth technique in SYMRAD for computing configuration factors is given by:

$$F_{ij} = \frac{1}{2\pi} \frac{2A_i A_j}{A_i S^4} (\hat{n}_i \cdot \vec{r}) (-\hat{n}_j \cdot \vec{r}) \quad (3.15)$$

where \vec{r} is the vector from the centroid of surface i to the centroid of surface j , $S = |\vec{r}|$, \hat{n}_i (\hat{n}_j) are the unit normal vectors of surfaces i (j), and A_i (A_j) are the areas of surfaces i (j).

Solutions using this method, called Method 4 in Section 9, improve in accuracy as the separation between surfaces i and j becomes larger. Sometimes referred to as the “five times rule” [8,9], an accuracy $\lesssim 2.5\%$ can be expected when the surfaces are separated by at least 5 surface element diameters. Results showing the dependence of the error on separation distance are shown in Table 9.3 for one of our benchmark problems. To obtain an accuracy of $\lesssim 0.1\%$ the separation distance should be $\gtrsim 20$ diameters.

Normalization

For a *closed environment*, the sum of the configuration factors for a given element i sums to unity:

$$\sum_j F_{ij} = 1 . \quad (3.16)$$

This simply states that when F_{ij} – i.e., the fraction of energy leaving surface element i that arrives at surface element j – is summed over all surfaces, the total must equal unity.

However, when the individual configuration factor integrals are numerically calculated, Eq. (3.16) is not satisfied exactly. For example, deviations of $\sim 10^{-3} - 10^{-2}$ (i.e., 0.1 – 1%) can be common. Therefore, in calculations involving enclosed surfaces, the user has the option of renormalizing the configuration fractions such that Eq. (3.16) is satisfied.

4. Self-Occultation Effects

When evaluating the configuration factors defined by Eq. (3.1), the integration is restricted to the cases when θ_i and θ_j are ≥ 0 . This is because each surface element has a “preferred” side from which radiation is emitted, which is in the direction of the unit normal vector. Before evaluating the configuration factor, F_{ij} , for a given i - j pair, we first check for blocking due to either “horizon effects” or intervening surface elements. Horizon effects refers to the occultation of radiation traveling between surfaces i and j by either surface i or j . Figure 4.1 shows an example of a case in which portions of surface j lie below the horizon of surface i .

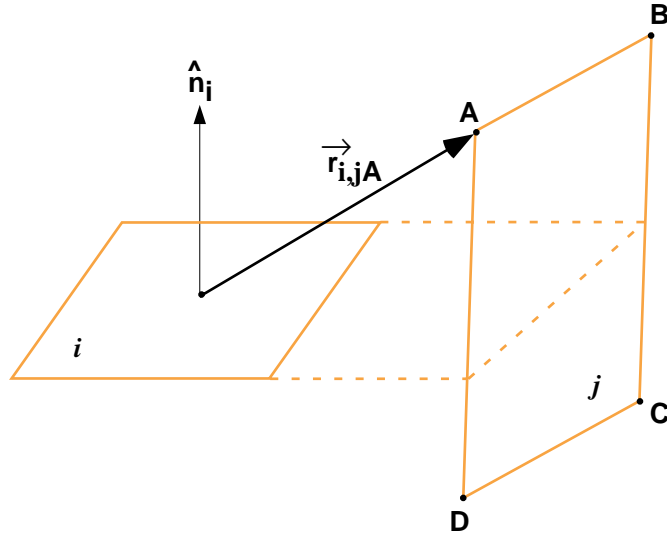


Figure 4.1. Schematic illustration showing blocking of radiation due to “horizon effects”.

If $\vec{r}_{i,jA}$ is the vector going from a point on surface i to vertex A of surface j , then vertex A_j is below the horizon of surface i if:

$$\hat{n}_i \cdot \vec{r}_{i,jA} < 0,$$

where \hat{n}_i is the unit normal vector of surface i . If all vertices of surface j are below surface i (or vice versa), then $F_{ij} = 0$, in which case the segment-to-segment configuration factor integrations are not performed. If all vertices of i are above the horizon of surface j ,

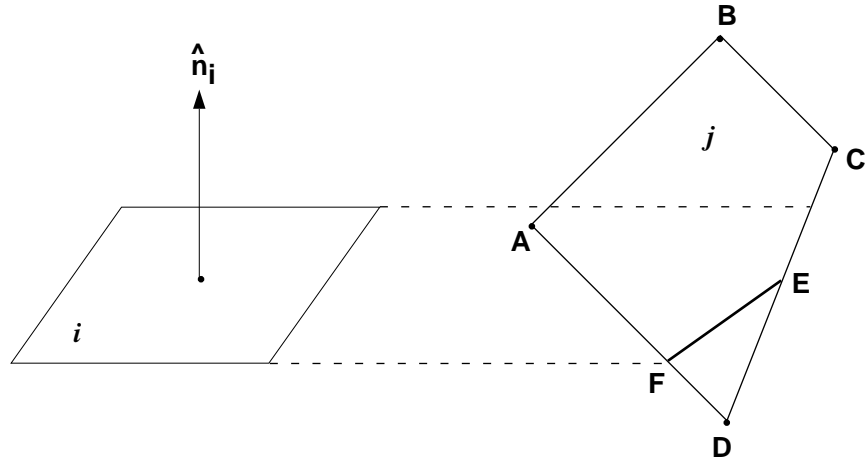


Figure 4.2. Schematic illustration showing how surface element boundaries are redefined in cases where blocking due to horizon effects occurs.

and all vertices of j are above the horizon of surface i , then there is no reduction of the configuration factor due to self-occultation effects.

Figure 4.2 shows a situation in which some vertices of surface j lie above the horizon of surface i , but at least one of the vertices lies below the horizon (in this case, point D). To evaluate the configuration factor in these situations, we redefine the original $ABCD$ boundary of surface j to a boundary defined by segments $ABCEFA$. Then the F_{ij} are accurately computed utilizing segment-to-segment contributions from the redefined boundary. In cases where Eq. (3.15) is used (Method 4), a new centroid position is calculated for the redefined polygon. As an example, Figure 4.3 shows all the surfaces (some with redefined boundaries) of a cylindrical hohlraum above the horizon of a surface element located on the capsule. The four plots represent different viewing angles, including along the hohlraum axis (upper left), and from a point near the (extended) plane of the surface element on the capsule (lower left). Surfaces and vertices which are shown lie above, or in the plane of, the horizon of the capsule surface element.

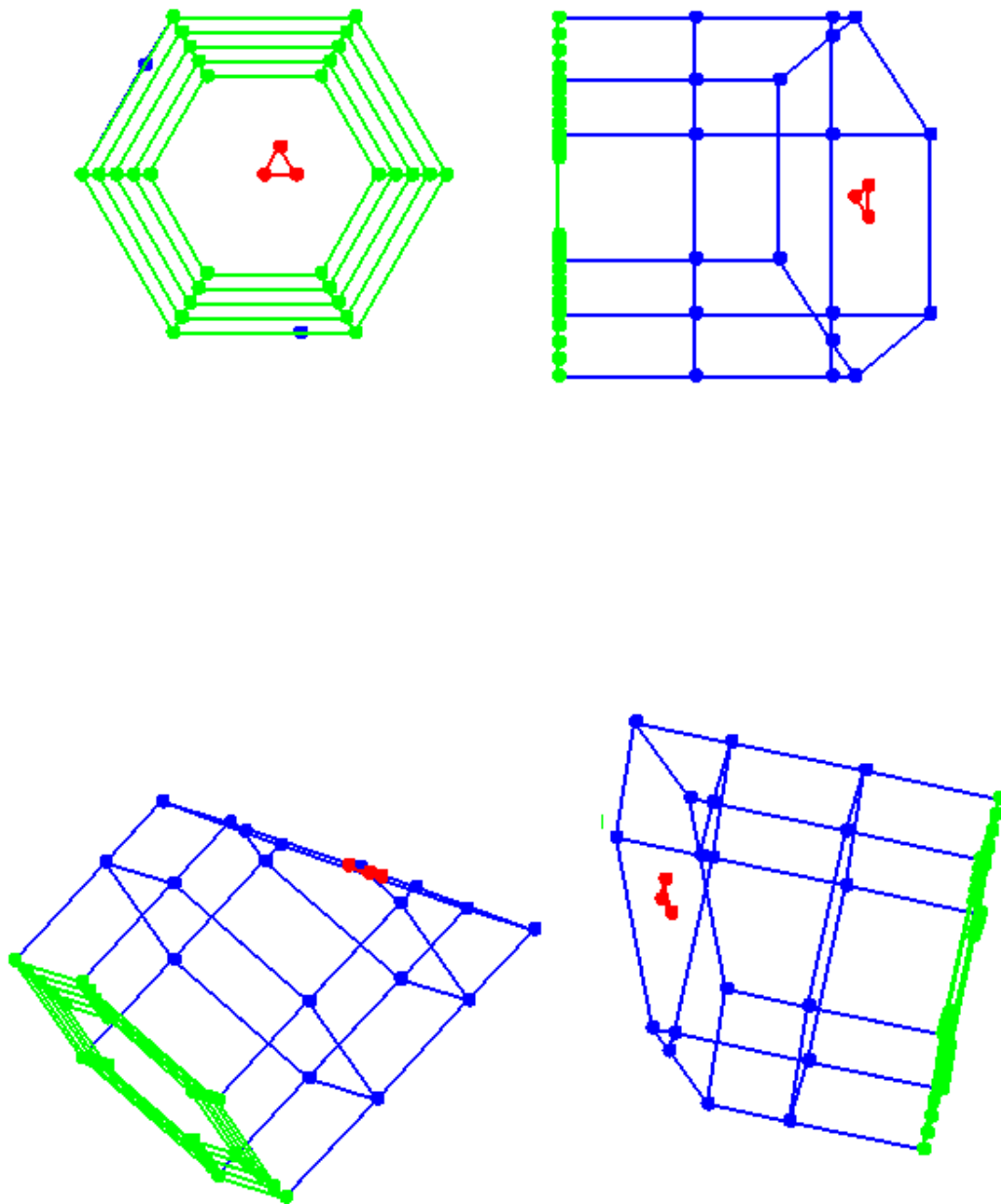


Figure 4.3. Surfaces and vertices which lie above, or in the plane of, a surface element located on the capsule (in red). Surfaces below the “horizon” of the capsule surface element are not shown.

5. Blocking By Intervening Surfaces

To determine the reduction in the configuration factor, F_{ij} , by “blocking” (or occultation) by a surface element lying between surfaces i and j , we use a ray-casting approach to test lines-of-sight (see, e.g., [11]). Let \mathbf{r}_i and \mathbf{r}_j define points lying on surfaces i and j , respectively (see Figure 5.1). Then, the equation of the line connecting these points can be written as:

$$\mathbf{r}(t) = \mathbf{r}_i + t \Delta\mathbf{r}_{ij} , \quad (5.1)$$

where

$$\Delta\mathbf{r}_{ij} = \mathbf{r}_j - \mathbf{r}_i .$$

Note that when $0 \leq t \leq 1$, $\mathbf{r}(t)$ lies between surfaces i and j . To determine if $\Delta\mathbf{r}_{ij}$ intersects surface k , we first determine the intersection point of the line defined by $\Delta\mathbf{r}_{ij}$ and the plane defined by surface k . The latter is given by:

$$n_x x + n_y y + n_z z = d , \quad (5.2)$$

where $\hat{n} = [n_x, n_y, n_z]$ is the unit normal vector for surface k . Solving for t gives:

$$t = \frac{d - \hat{n} \cdot \mathbf{r}_i}{\hat{n} \cdot \Delta\mathbf{r}_{ij}} . \quad (5.3)$$

If $t < 0$ or $t > 1$, the extended plane defined by surface k does not intersect the portion of the line between \mathbf{r}_i and \mathbf{r}_j . Similarly, if $\hat{n} \cdot \Delta\mathbf{r}_{ij} = 0$, the line and plane are parallel and there is no intersection.

If $0 < t < 1$, we must check to see where the intersection point lies on surface k , which in Figure 5.1 is bounded by vertices $ABCD$. Letting P define the intersection point, we can write:

$$\vec{AP} = \alpha \cdot \vec{AB} + \beta \cdot \vec{AC} . \quad (5.4)$$

Then P is inside of the triangle defined by vertices ABC if and only if (see, e.g., [11]):

$$\alpha \geq 0$$

$$\beta \geq 0$$

and

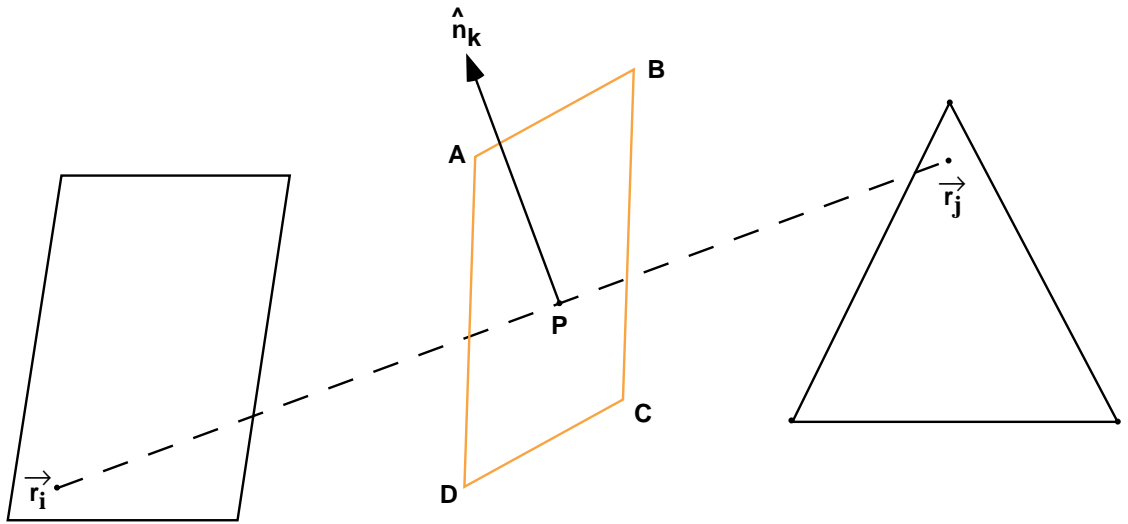


Figure 5.1. Schematic illustration of ray-casting approach for testing whether an intervening surface interrupts the line-of-sight between two other surface elements.

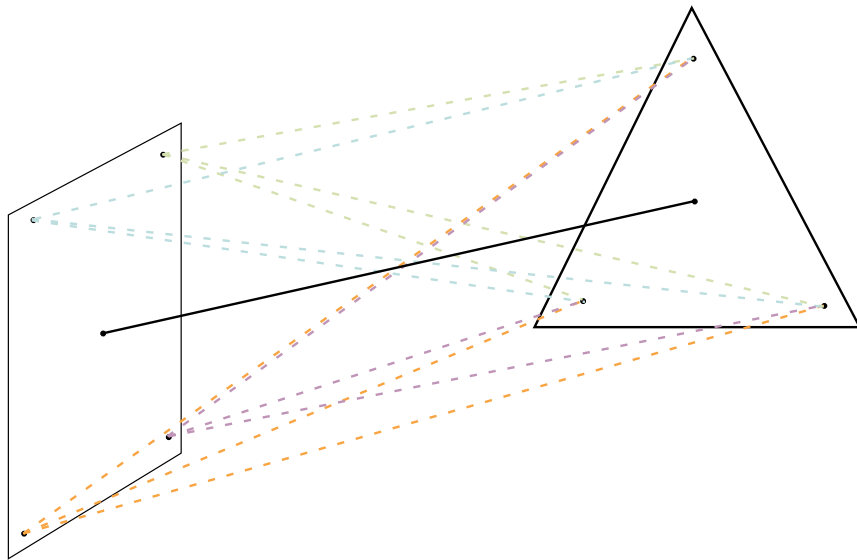


Figure 5.2. Illustration showing multiple line-of-sight tests for evaluating “blocking” of radiation by intervening surface.

$$\alpha + \beta \leq 1.$$

In cases where surface k is a quadrilateral, a second test is made to see if the intersection point is inside triangle ACD .

The above procedure allows us to efficiently determine whether a single line segment between points lying on two surfaces is intersected by a third polygon. In SYMRAD, one has the option of using a single line-of-sight test between surfaces, or testing multiple lines-of-sight. In the latter case, we utilize test points which are located near the polygon vertices (see Figure 5.2). Thus, in addition to the centroid-to-centroid test, (near-) vertex-to-vertex line-of-sight pairs are also checked. The resultant configuration factor is then reduced by the fractional number of lines-of-sight which are not intersected by an intervening surface. That is:

$$F_{ij} = \frac{N_U}{N_{LOS}} F_{ij}^0, \quad (5.5)$$

where F_{ij}^0 is the unoccluded value of the configuration factor, N_U is the number of unblocked lines-of-sight, and N_{LOS} is the number of line-of-sight tests performed. When $N_U = 0$, the transmission fraction is zero and the configuration integrals for F_{ij} are not evaluated.

To save computational time, an option has been added so that the user can specify which objects can block radiation emitted by other objects. As an example, we know that the radiation emitted by the capsule is not blocked by any other object (e.g., hohlraum cylinder, end caps) in a typical ICF experiment. Thus, one can potentially realize a considerable savings in CPU time by not performing line-of-sight tests for all surface elements of the hohlraum wall. This option has been added to SYMRAD. By default, all surfaces will be checked as potential blockers.

6. Solution of the Radiosity Equation

The “radiosity equation” describes the relationship between the surface emission, absorption, and source terms. It simply balances the radiative power emitted by a surface with the power absorbed by that surface and the power input from other non-radiative sources (e.g., laser beams). It can be written as:

$$B_i - \alpha_i \sum_j F_{ij} B_j = E_i, \quad (6.1)$$

where B_i is the “radiosity” of surface i , α_i is the reflectivity, or albedo, of surface i , E_i is the source term, and F_{ij} is the occultation-corrected configuration factor. Physically, B_i is the energy radiated per unit area per unit time from surface i . It can be thought of as $B_i = \sigma T_{e,i}^4$, where $T_{e,i}$ is the “electron temperature”, or “emission temperature”. The total radiative flux going onto surface i due to radiation from all other surfaces is:

$$q_i^{in} = \sum_j F_{ij} B_j.$$

This can also be used to define a “radiation temperature” at surface i :

$$q_i^{in} = \sigma T_{R,i}^4.$$

Calculation of the source terms is described in Section 7.

The configuration factors in Eq. (6.1) depend only on the geometry of the individual surfaces. The source terms are generally computed using the laser ray-trace model (or simpler models if desired), and the albedos can be either defined by the user through namelist input or be calculated from radiation-hydrodynamics simulations. Thus, given E_i , α_i , and F_{ij} , the radiosity equation is simply a matrix equation which can be inverted to provide B_i for all surfaces. In SYMRAD this matrix inversion can be performed by calling LAPACK routines [12].

Alternatively, one can solve Eq. (6.1) using an iterative procedure. This can be useful in cases where the total number of surfaces is very large. In this case, an initial estimate is made for B_i . Then on each successive iteration the B_i are updated using:

$$B_i^{(k+1)} = E_i + \alpha_i \sum_j F_{ij} B_j^{(k)},$$

where the superscript k refers to the iteration cycle. An option to use successive over-relaxation has also been included to improve convergence.

7. Laser Deposition Ray-Trace Algorithm

Laser energy deposition into the hohlraum is modeled using a 3-D ray-trace algorithm. In this approach, each laser beam is divided into a specified number ($\sim 10^2$) of beamlets. At present, each beamlet in a given beam is assumed to have the same power: $P_L(t)/N_{BL}$, where $P_L(t)$ is the time-dependent power of the beam and N_{BL} is the number of beamlets in a given beam. Each beamlet is treated as a ray, which originates from a beam port on the target chamber. The laser power incident on a given surface element of a hohlraum is determined by the number and power of beamlet rays which hit the surface element.

Figure 7.1 shows how the beamlets are distributed within a given beam. The direction of the beam (\vec{D}_L) is determined by the position of the laser port in the target chamber wall and the focal point (F). The position of the focal point is generally specified in a coordinate system defined by a laser entrance hole (LEH). (This is discussed in greater detail below.) Vectors specifying the direction of the beamlet propagation are defined by 2 points: the focal point, F , and a point on an imaginary plane which is normal to \vec{D}_L . The intersection of the conical laser beam and the imaginary plane is represented by the two circles shown in Figure 7.1, where the pattern of beamlet intersection points is represented by the dots. Note that in both dimensions of the plane, the spacing between adjacent beamlets is identical. Thus, in a situation where a laser beam irradiates a surface which is normal to the incident beam, the incident power density (TW/cm²) is uniform. The angles θ_{min} and θ_{max} define the opening angle of the beam. When $\theta_{min} > 0$, the laser is represented as a hollow cone.

In laser hohlraum simulations, the position of the focal point can be defined relative to the center of laser entrance holes. By default, F for each laser beam is specified as the center of the LEH which is closest to the target chamber laser port of that beam. Offsets to this default position can be specified in a coordinate system in which the origin is at the center of the LEH, and the z-axis runs through the origin of the target coordinate system and the LEH center point (see Figure 7.2). Thus, one can, for example, readily specify that F is located a given distance at a point just outside the LEH. It is also possible to specify F to be off of the LEH z-axis a distance Δr and rotation angle $\Delta\phi$. It may also be advantageous in the future to add a user-friendly graphically-based interface for repositioning the laser focal points.

Figure 7.3 shows an example of the intersection of the NOVA laser beams with a cylindrical hohlraum. The top image shows the view as seen from the location of the capsule, while the lower image is a view from outside of the hohlraum. The focal point F

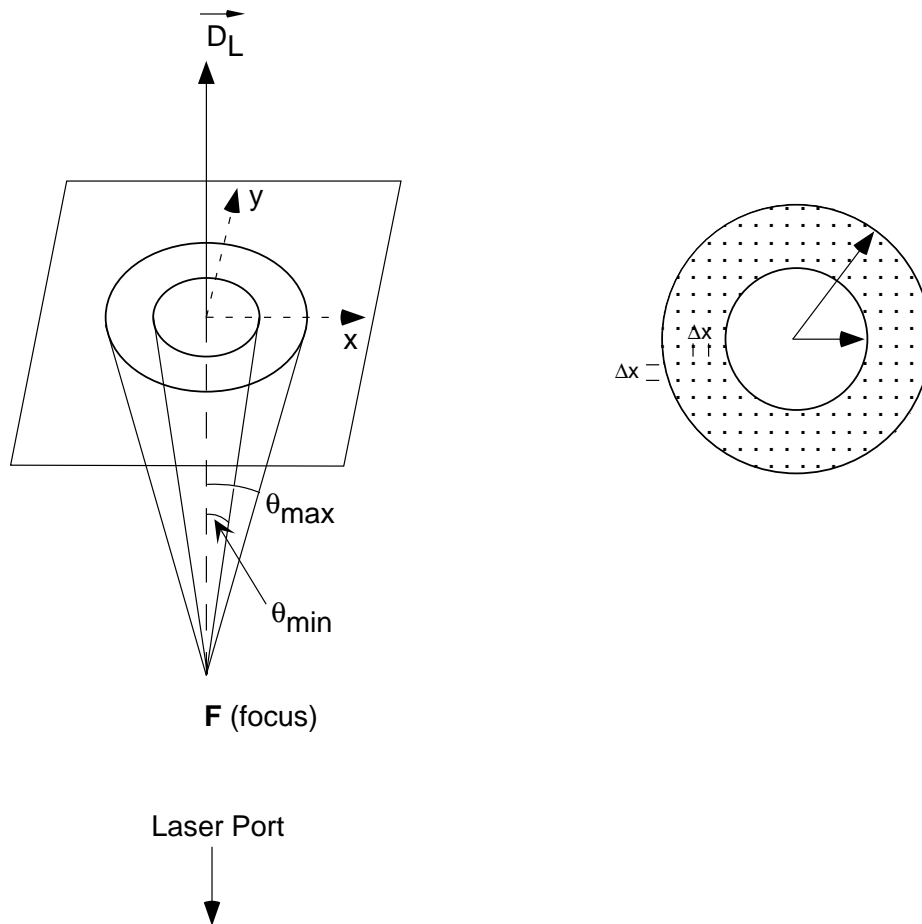


Figure 7.1. (Left) Illustration of conical laser beam passing through an imaginary plane which is perpendicular to the direction of propagation (\vec{D}_L) for the overall beam. (Right) Illustration of the intersections of beamlet rays of a conical hollow beam with imaginary plane.

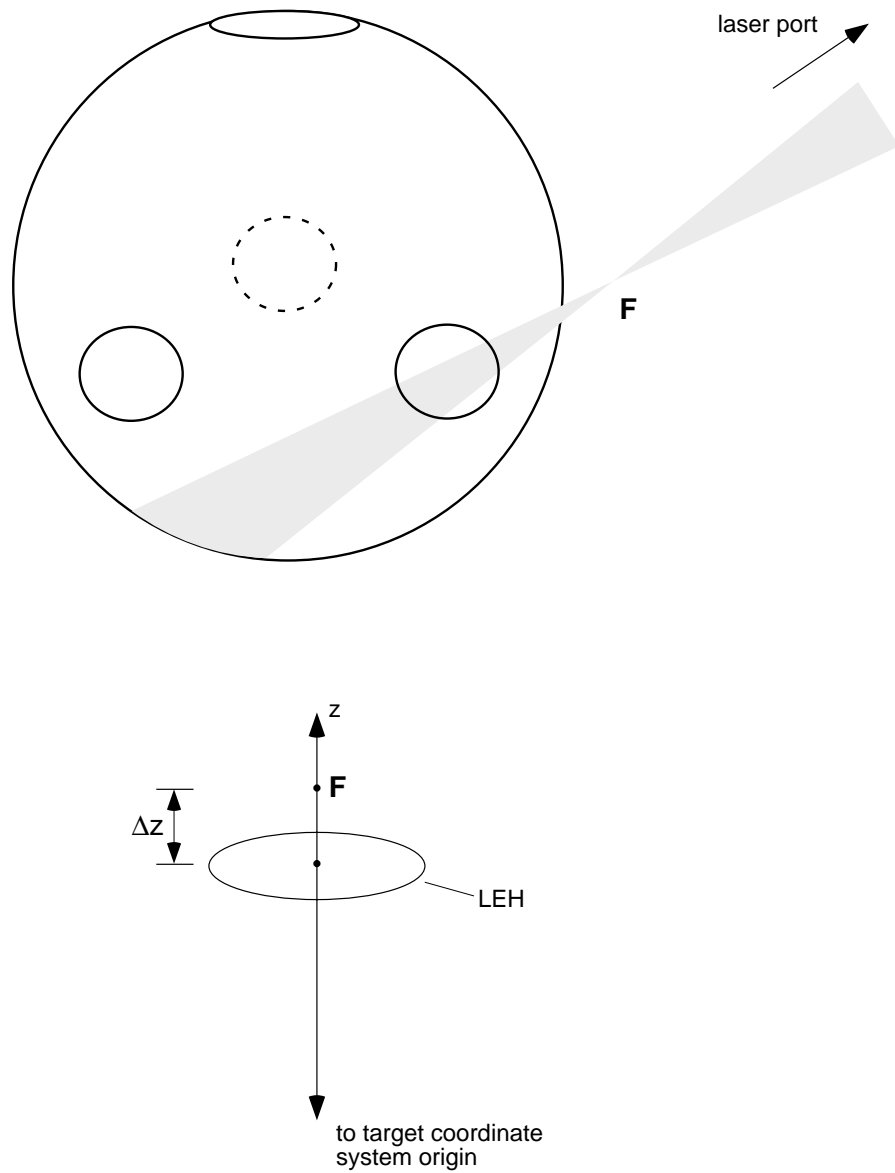


Figure 7.2. (Top) Illustration of a laser beam passing through one of the LEH in a tetrahedral hohlraum. The conical beam is modeled as a group of “beamlet” rays that fill the cone. The pointing of the beam is defined by its laser port on the target chamber wall and the focal point (F). (Bottom) Illustration showing how the position of the focal point (F) is prescribed in the coordinate system of the LEH.

is this case is assumed to be at the center of the LEH. The individual lines represent the beamlets used to model each of the beams, and the yellow dots represent the intersection points of the beamlet rays and the surface elements.

The intersection of laser beamlet rays with surface elements is accomplished using a procedure similar to that in testing intervening surface occultation effects (see Section 5). In this case, we need to identify the intersecting surface which is closest to the laser focal point. This is done by tracking the values of t in Eq. (5.3) in which a beamlet intersects a surface element. The lowest value of t indicates the nearest intersecting surface element.

The total incident laser power density on surface element i is:

$$PD_i = \sum_{j=1}^{N_L} \frac{M_{ji}}{N_{BL,j}} P_{L,j}(t) (1 - f_{scat}) \quad , \quad (7.1)$$

where the sum is over all N_L laser beams, $P_{L,j}(t)$ is the power of laser beam j at time t , f_{scat} represents the fraction of laser beam energy which is scattered back out of the hohlraum, and M_{ji} represents the number of beamlets of beam j striking surface element i . This power density goes into the source term in Eq. (6.1).

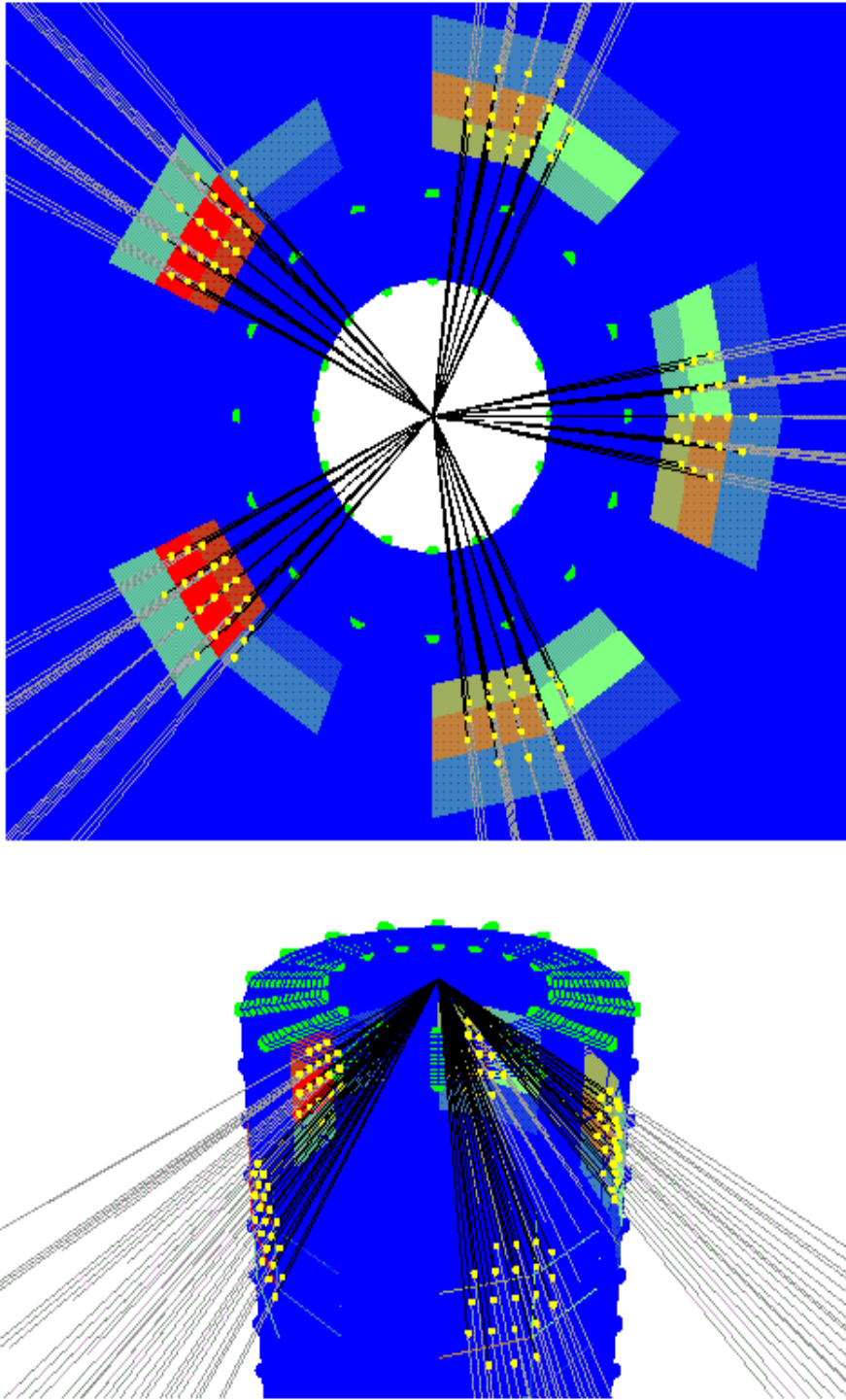


Figure 7.3. Example of NOVA laser beams entering a cylindrical hohlraum. The intersections of the individual beamlets and the hohlraum surface elements are represented by the yellow dots. The colored patches represent surfaces which are heated by the laser beams. (Top) View from the location of the capsule. (Bottom) View from outside the hohlraum.

8. Graphics

At present, SYMRAD uses the OPENGL [13] 3-D graphics library. Originally developed for Silicon Graphics workstations, OPENGL is available for a variety of platforms, including Windows-based PC's and, for a cost, HP workstations. An OPENGL clone, called MESA [14], is also available at no cost. MESA has been developed to run on a variety of Unix-based workstations. We have chosen to utilize OPENGL/MESA graphics libraries both because they are easy to use and because they should readily allow SYMRAD to be run on a variety of platforms.

Examples of the graphical output from SYMRAD are shown in Figures 2.1, 2.2, 4.3, and 7.3. These 3-D graphics libraries are also interactive; that is, the user can conveniently rotate objects, as well as “walk through” the objects in the problem geometry. To date, the graphics algorithms in SYMRAD have been used primarily as an instrument for debugging. More sophisticated “presentation quality” graphics algorithms should be implemented in future versions of SYMRAD.

9. Benchmark Calculations

9.1. Evaluation of Different Configuration Factor Integration Methods

To assess the accuracy and computational efficiency of the different integration methods for evaluating surface-to-surface configuration factors, we performed benchmark calculations for three problems which have analytic solutions. The three benchmark problems are illustrated in Figure 9.1. They are: (1) two parallel plates of finite extension; (2) two perpendicular plates of finite extension with a common edge; and (3) two infinitely long plates with a common edge at angle α . All three surface geometries have analytic solutions which are given in Appendix C of Ref.[10].

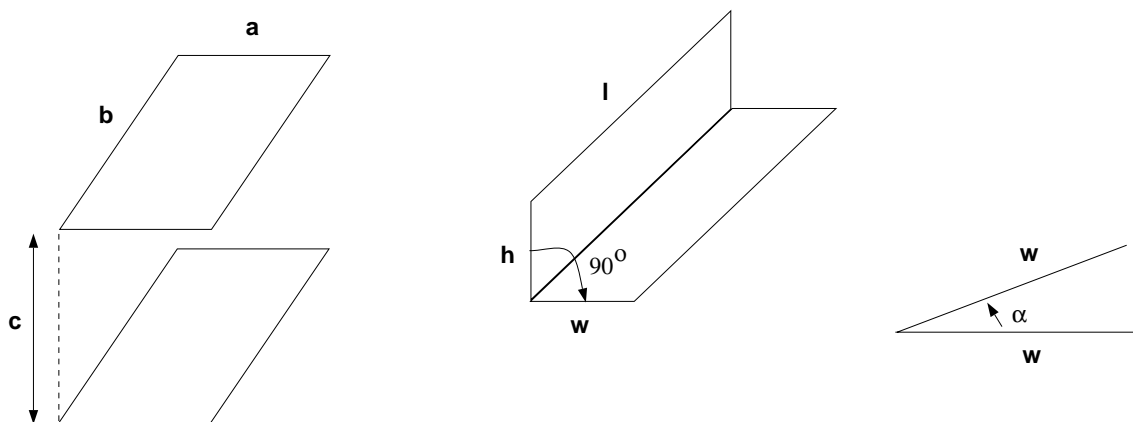


Figure 9.1. Illustration of benchmark calculation surface geometries used in testing configuration factor integration methods.

Table 9.1 shows results for two sets of calculations for two parallel plates with parameters $a = 5$, $b = 3$, $c = 0.01$ and $a = 5$, $b = 3$, $c = 5$. In the former case, the distance separating the plates is small compared to the plate areas. This provides a more rigorous test for the configuration factor integration algorithms. (Note that in these three benchmark calculations the plates are not subdivided into smaller surface elements.) Methods 1 through 4 are defined in Section 3. For Methods 1, 2, and 3, the percent errors decrease as the number of subsegments (i.e., integration points along

each segment bounding a surface) increases. Methods 2 and 3 provide the best accuracy. Method 4 is least accurate, and as pointed out previously [8], should only be used when the separation between the surface is large compared to the size of each surface. Note that for Methods 2 and 3, the accuracy is better than 1% when the number of integration points is ≥ 2 for $c = 5$ and ≥ 5 for $c = 0.01$.

Timing studies were also done for this problem to assess the relative computational efficiencies of these methods. Results are shown in Table 9.2 for cases with 3 integration points and 10 integration points per segment. Clearly the fastest method is Method 4. However, this method is not accurate when surfaces are close together. Table 9.3 shows the accuracy of Method 4 as a function of plate separation. Note that 1% accuracy is not achieved until $c \gtrsim 40$; that is, $c/\sqrt{ba} \gtrsim 0.1$. Method 1, because it performs a numerical integration for both portions of the configuration factor double integral, exhibits a significant increase in CPU time as the number of integration points increases. Thus, this method can often be both less accurate and less efficient than Methods 2 and 3. This is interesting because Method 1 is often used in view factor codes.

Tables 9.4 and 9.5 show results from benchmark simulations corresponding to Figures 9.1(b) and 9.1(c). Again, we find Methods 2 and 3 provide much better accuracy than Methods 1 and 4. Table 9.5 results also show Method 3 is significantly more accurate than Method 2 for this class of problems. In most of the test results shown, Method 3 provided an accuracy of better than 1% when $\gtrsim 10$ integration points per segment were utilized. The sole exception to this is in Table 9.5 for the $\alpha = 170^\circ$ case. However, it is important to note that in this particular case, the magnitude of F_{ij} is much smaller. Thus, its contribution to the overall radiation field is very small.

Based on the above calculations, we conclude that Method 3, which solves the configuration factor double integral analytically to the maximum extent possible, provides the overall best accuracy for evaluating configuration factors, and does so with relatively good computational efficiency.

9.2. Concentric Sphere Benchmark Calculations

A series of concentric sphere benchmark calculations was also performed to assess the accuracy of the SYMRAD code. In these problems, the goal is to compute the flux distribution incident on the inner sphere due to radiation emitted from the inner surface of the outer sphere. The radiative flux emitted by the outer sphere is azimuthally symmetric, but has a prescribed polar asymmetry.

Table 9.1. Results from Parallel Plate Benchmark Calculation

Case A: a = 5, b = 3, c = 0.01				
Number of Subsegments	Percent Error in F_{12}			
	Method 1	Method 2	Method 3	Method 4
1	400	10.3	4.5	5e6
2	140	3.7	0.99	5e6
3	80	1.9	0.42	5e6
5	40	0.81	0.15	5e6
10	15	0.24	0.035	5e6
100	0.21	0.003	-0.0001	5e6
Case B: a = 5, b = 3, c = 5				
Number of Subsegments				
	Method 1	Method 2	Method 3	Method 4
1	8.4	3.6	-4.9	40
2	1.7	0.81	-1.0	40
3	0.71	0.35	-0.43	40
5	0.25	0.13	-0.15	40
10	0.063	0.031	-0.038	40
100	0.0006	0.0003	-0.0004	40

Table 9.2. Results of CPU Time Studies

CPU Times* per $10^5 F_{ij}$ Calculations (seconds)				
Number of Subsegments				
	Method 1	Method 2	Method 3	Method 4
3	32	44	42	9
10	168	78	65	9

*Calculations performed on a HP 735 Workstation.

Table 9.3. Accuracy of Method 4 Model ($a = 5, b = 3$)

c	% Error
.01	5e6
.1	5e4
1	680
3	100
5	40
10	11
30	1.3
50	0.45
100	0.11

Table 9.4. Results from Perpendicular Plate Benchmark Calculation

$\ell = 8, w = 4, h = 2$				
Number of Subsegments	Percent Error in F_{12}			
	Method 1	Method 2	Method 3	Method 4
2	-18	-6.5	4.6	144
3	-6.3	-2.8	2.0	144
5	-2.0	-1.0	0.65	144
10	-0.48	-0.24	0.16	144
100	-0.0048	-0.0024	0.0016	144

Table 9.5. Results from Benchmark Calculation with Two Plates Adjoining at Angle α

w = 0.5, L = 100 (L/w $\rightarrow \infty$)						
Number of Subsegments	α	Percent Error in F_{12}				$2\pi A_1 F_{12}$ (exact)
		Method 1	Method 2	Method 3	Method 4	
3	10°	-1e3	-110	1.1	9e5	286.8
10	10°	84	-13	0.66	9e5	286.8
100	10°	27	-0.16	0.024	9e5	286.8
3	90°	-1e4	-340	0.18	2e4	92.02
10	90°	-2e3	-42	0.18	2e4	92.02
100	90°	-9.6	-0.72	-0.83	2e4	92.02
3	170°	-9e4	-3e4	-150	1e4	1.196
10	170°	-2e5	-3e3	-57	1e4	1.196
100	170°	-810	-43	8.3	1e4	1.196

In the first set of concentric sphere calculations, we compare our results with those previously obtained [15] using a LANL view factor code [16]. In this case, the source distribution, $q_s(\theta)$, at the outer sphere is given by:

$$q_s(\theta) = q_s^* (1 + \beta_2 P_2(\cos \theta)), \quad (9.1)$$

where θ is the polar angle, q_s^* is a constant, $P_2(\cos \theta)$ is the second Legendre polynomial ($P_2(x) = \frac{3}{2}x^2 - \frac{1}{2}$), and β_2 is a constant. Note that the ratio of the minimum to maximum flux is given by:

$$\varepsilon_0^4 = \frac{1 - \frac{1}{2}\beta_2}{1 + \beta_2}.$$

In the calculations discussed below, we assume $\beta_2 = 0.950$, so that $\varepsilon_0 = 0.720$.

We first considered the case where both spheres are perfect absorbers; that is, both the albedo of the inner sphere (α_i) and outer sphere (α_0) are zero. In this case, it is possible to readily evaluate the incident flux at a point on the inner sphere by direct numerical integration:

$$\mathfrak{S}(\theta_i) = \int_0^{2\pi} d\alpha \int_0^1 d\mu \mu B_0 (1 + \beta_2 P_2(\mu)) , \quad (9.2)$$

where $\mu = \cos(\gamma)$, γ is the polar angle of a point on the outer (emitting) sphere relative to the point on the inner sphere at polar angle θ_i (see Figure 9.2), α is the azimuthal angle in the coordinate system defined by the point on the inner sphere, and B_0 is a constant ($\sim \sigma T^4$).

Results for the flux distribution on the inner sphere are shown in Figure 9.3 as a function of polar angle for cases of $\eta (= R_{inner}/R_{outer}) = 0.5$ and $\eta \rightarrow 0$. The SYMRAD results (squares) are seen to compare favorably with the direct numerical integration results (solid curve).

As an additional check, we compared the total “sphere-to-sphere” configuration factors with analytic solutions. For two concentric spheres, the fraction of radiation emitted by the outer sphere that arrives at the inner sphere is:

$$F_{oi} = (R_{inner}/R_{outer})^2 , \quad (9.3)$$

while the remaining fraction that arrives at other points on the outer sphere is:

$$F_{oo} = 1 - (R_{inner}/R_{outer})^2 , \quad (9.4)$$

where the R 's represent the radii of each sphere. Table 9.6 compares the SYMRAD results using a total of 1040 surface elements with exact solutions. The SYMRAD results are seen to be in good agreement with the exact values, with typical errors being a fraction of 1%.

A series of concentric sphere calculations were performed to compare with previous solutions calculated using a LANL code [15,16]. Figure 9.4 shows SYMRAD results for a variety of inner sphere and outer sphere albedos as a function of the ratio of the sphere radii (R_i/R_o). Also shown are LANL code results (solid and dashed curves), which are based on curve fits to the results of numerical view factor calculations [15], and for the case of $\alpha_i = \alpha_o = 0$, results from direct numerical integration of the flux equation (Eq. (9.2)) (represented by the lower open squares). Results for the $\alpha_i = \alpha_o = 0$ case are also listed in Table 9.7.

We find that discrepancies between the SYMRAD and LANL results range up to $\sim 20\%$, with the LANL results predicting a larger ratio of F_{min}/F_{max} in most cases. On the other hand, for the $\alpha_i = \alpha_o = 0$ cases (lower curve and points in Figure 9.4), the SYMRAD results compare favorably with the flux ratio computed by direct numerical integration. In these calculations, the agreement is good to within 1 – 2 %.

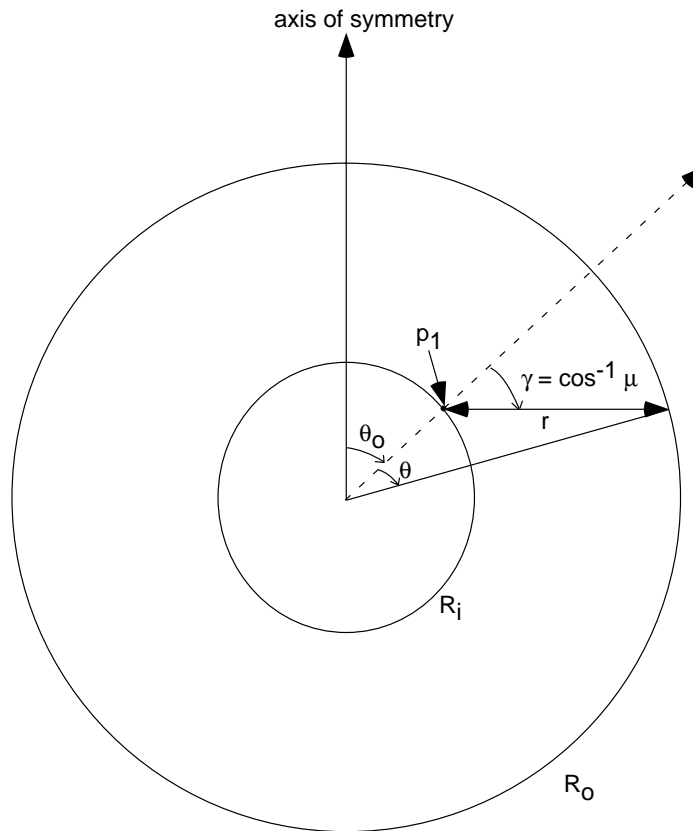


Figure 9.2. Concentric sphere coordinate geometry.

Concentric Spheres Benchmark Problem

$$\alpha_{\text{outer}} = \alpha_{\text{inner}} = 0.0 ; \epsilon_o = 0.72$$

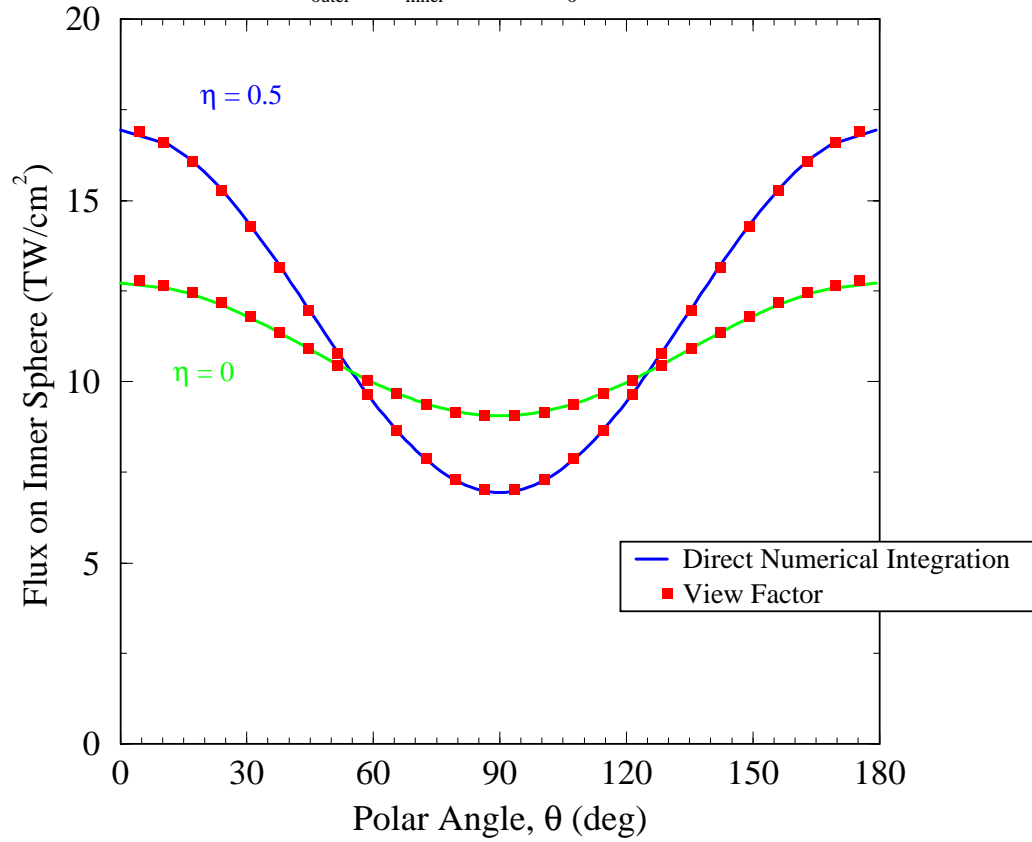


Figure 9.3. Comparison of incident flux distributions calculated using SYMRAD and from direct numerical integration of Eq. (9.2). η is the ratio of the inner sphere radius to the outer sphere radius.

Table 9.6. Total Object Configuration Factors from Concentric Spheres Benchmark Calculations

R_i/R_0	F_{oi} (calc.)	F_{oi} (exact)	F_{00} (calc.)	F_{00} (exact)
0.01	1.002×10^{-4}	1.00×10^{-4}	0.9999	0.9999
0.5	0.2514	0.2500	0.7486	0.7500
0.8	0.6415	0.6400	0.3585	0.3600

Table 9.7. Concentric Sphere Benchmark Results for $\alpha_i = \alpha_0 = 0$

Flux (min) / Flux (max)				
R_i/R_0	SYMRAD	LANL	Numerial Integration	Analytic
0	-	0.708	0.712	0.712
0.01	0.708	0.703	0.705	-
0.3	0.517	0.576	0.513	-
0.5	0.415	0.488	0.410	-
0.8	0.308	0.357	0.302	-

Concentric Spheres Benchmark Problem

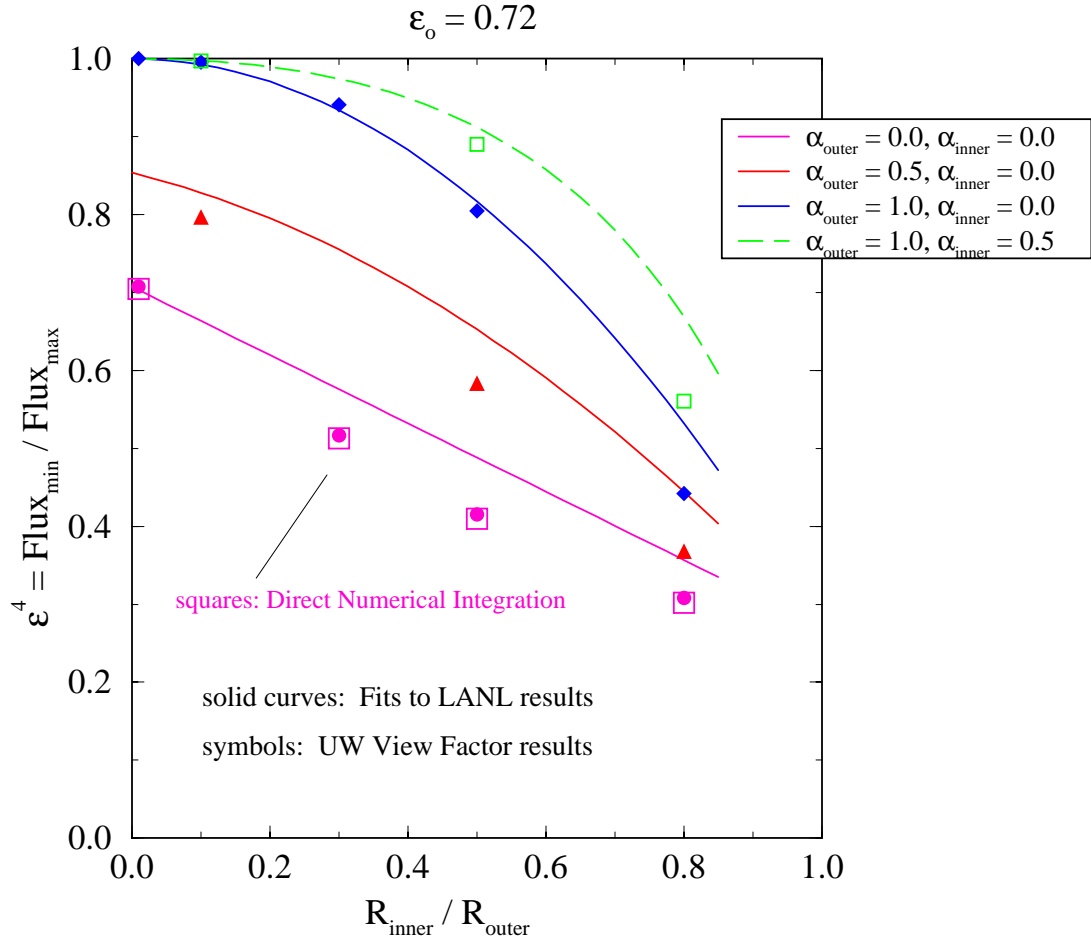


Figure 9.4. Comparison of SYMRAD (symbols) and LANL (solid and dashed curves) results from concentric sphere benchmark calculations. Results are shown for several values of α_i and α_o . Also shown are results from the direct numerical integration of Eq. (9.2).

As an additional series of tests, we compared the results from SYMRAD concentric sphere calculations with those obtained using the Legendre polynomial expansion method of Haan [17]. In these simulations, the spheres have zero albedos, and the flux (emission source) distribution on the outer sphere is represented in a more general form as:

$$\mathfrak{S} = \mathfrak{S}_0 \sum_{\ell=0}^{\infty} t_{\ell} P_{\ell}(\cos \theta_0) P_{\ell}(\cos \theta) , \quad (9.5)$$

where \mathfrak{S}_0 is a constant, t_{ℓ} is a user-specified constant, and θ_0 is the angle between the axis of symmetry and a point on the inner sphere (p_1 in Figure 9.2). Following the approach of Haan, we note the following relationships:

$$\cos \theta = \frac{1 + \eta^2 - z}{2\eta} , \quad (9.6)$$

$$\mu = \cos \gamma = \frac{1 - \eta^2 - z}{2\eta\sqrt{z}} , \quad (9.7)$$

and

$$2\mu d\mu = dz \frac{1}{4\eta^2} \left[1 - \frac{(1 - \eta^2)^2}{z^2} \right] , \quad (9.8)$$

where $\eta = R_i/R_0$ and $z = (r/R_0)^2$. Solving for the flux at p_1 gives:

$$\mathfrak{S}(p_1) = \mathfrak{S}_0 \sum_{\ell=0}^{\infty} t_{\ell} P_{\ell}(\cos \theta_0) f_{\ell}(\eta) , \quad (9.9)$$

where

$$f_{\ell}(\eta) = \frac{1}{4\eta^2} \int_{(1-\eta)^2}^{(1+\eta)^2} dz \left[\frac{(1 - \eta^2)^2}{z^2} - 1 \right] P_{\ell} \left(\frac{1 + \eta^2 - z}{2\eta} \right) . \quad (9.10)$$

In SYMRAD, we have added subroutines to compute $f_{\ell}(\eta)$ numerically, as well as the flux at an arbitrary point on the inner sphere. Results of $f_{\ell}(\eta)$ were compared with Table 1 in Haan [17], and in all instances we found complete agreement to the 5 significant figures shown in his table.

Results for several assumed temperature distributions are shown in Figures 9.5 through 9.9. Unless otherwise noted, the parameters in these calculations were as

follows: $R_i/R_0 = 0.7$; the number of azimuthal grid points, N_ϕ , was 14 for each sphere; the number of polar grid points, N_θ , was 27 for each sphere (for this N_ϕ and N_θ , the total number of surfaces was 782); the number of subsegments used in the numerical integration portion of the configuration factor integral was 10. A relatively large value of R_i/R_0 was used to enhance the angular dependence of the results.

Figure 9.5 shows results for $t_\ell = 0.5$ ($t_{\ell \neq 1} = 0$). (Note that in all cases $t_0 = 1$.) The flux on the inner sphere calculated using SYMRAD and Haan’s formula is shown in the top plot. The percent error, defined as

$$\Delta(\%) = 100 \cdot \left[\frac{Flux_{SYMRAD} - Flux_{Haan}}{Flux_{Haan}} \right] , \quad (9.11)$$

is shown in the bottom plot. For this P_1 asymmetry, our view factor results are accurate to $\leq 0.4\%$.

Figure 9.6 shows results for a P_3 temperature distribution ($t_3 = 1, t_{\ell \neq 3} = 0$). In this case, the maximum error is 1.3 %. Results for a P_4 are shown in Figure 9.7. In the bottom plot, the solid curve shows results for the “baseline” case with $N_\phi = 14$ and $N_\theta = 27$. In this case the maximum error is seen to be 1.1%. Also shown are results for $N_\theta = 43$ and $N_\theta = 13$ (with $N_\phi = 14$) and $N_\phi = 23$ (with $N_\theta = 27$). Decreasing the number of polar angle grid points to $N_\theta = 13$ results in significantly larger errors (up to 3.6%). Increasing N_θ to 43 points reduced the maximum error to 0.78%. Finally, increasing N_ϕ to 23 points leads to a maximum error of 0.88%. Note that the errors are small compared to the total change in flux across the inner sphere, which is slightly more than a factor of 2.

It is also interesting to examine a case where the magnitude of the asymmetry is small. An example of this is shown in Figure 9.8, where R_i/R_0 is 0.3 and $t_4 = 0.2$. In this case, the ratio of the maximum to minimum flux is 1.016; that is, about 1.6% of the total flux. By comparison, the errors are typically $\leq 0.1\%$.

Finally, Figure 9.9 shows results for a P_2 asymmetry ($t_2 = 0.95, t_{\ell \neq 2} = 0$) with $R_i/R_0 = 0.3$. These parameters are more typical for ICF experiments. In the baseline case (solid curve), the maximum error is seen to be 0.8%. However, by increasing N_ϕ from 14 points to 21 points, the maximum error drops to 0.4%. We note that by increasing the number of subsegments from 10 to 30 had no noticeable effect. That is, the errors in computing the view factors (i.e., the configuration factor integrals) are small compared to those introduced by modeling the spheres as a finite number ($\sim 10^2 - 10^3$) of polygons.

Concentric Spheres Benchmark Problem

$$\alpha_{\text{outer}} = \alpha_{\text{inner}} = 0.0 ; R_i/R_o = 0.7 ; t_1 = 0.5$$

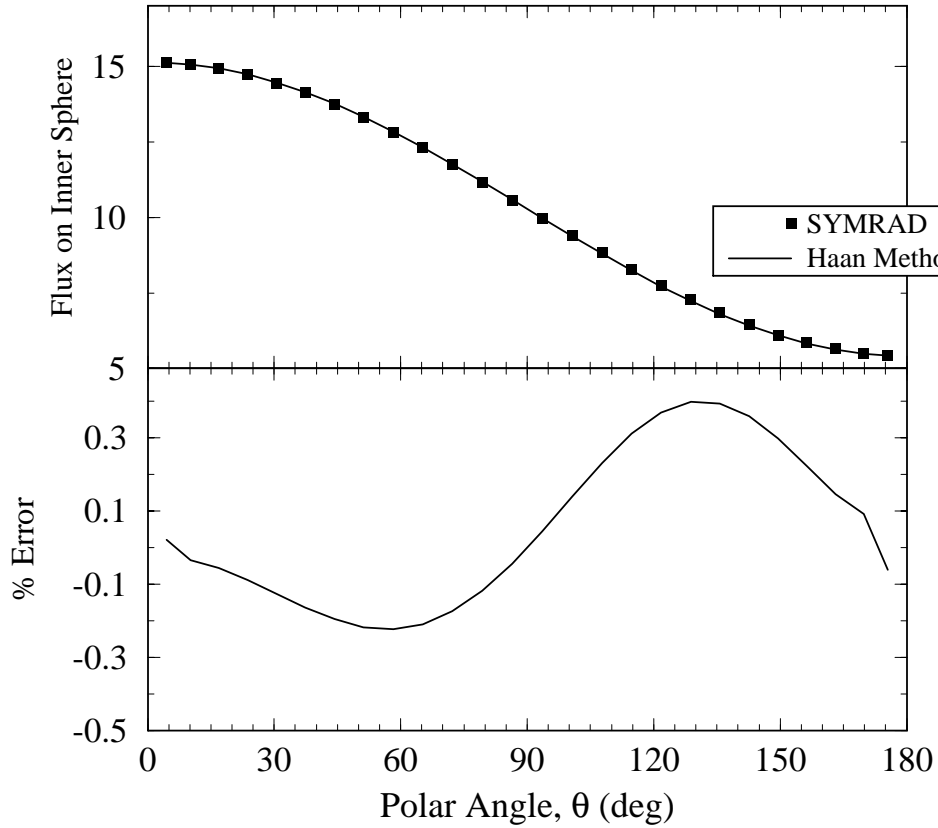


Figure 9.5. Comparison of incident flux distributions on inner sphere calculated using SYMRAD and from Haan's method for a P_1 source distribution.

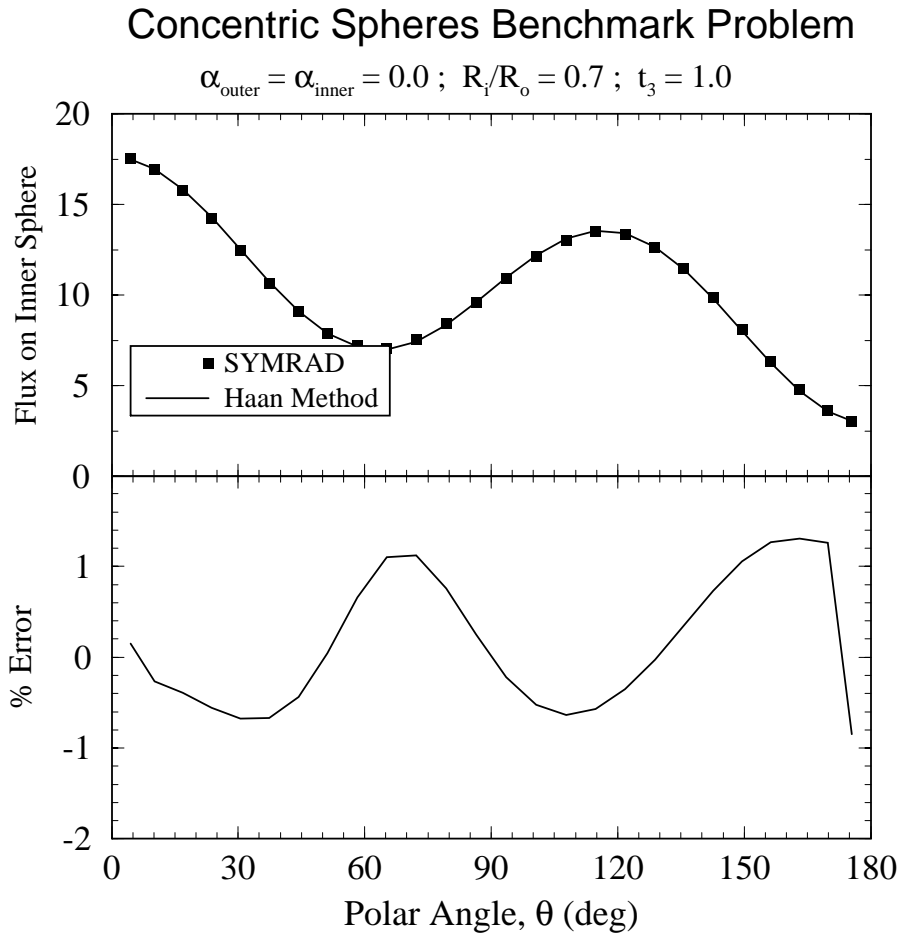


Figure 9.6. Comparison of incident flux distributions on inner sphere calculated using SYMRAD and from Haan's method for a P_3 source distribution.

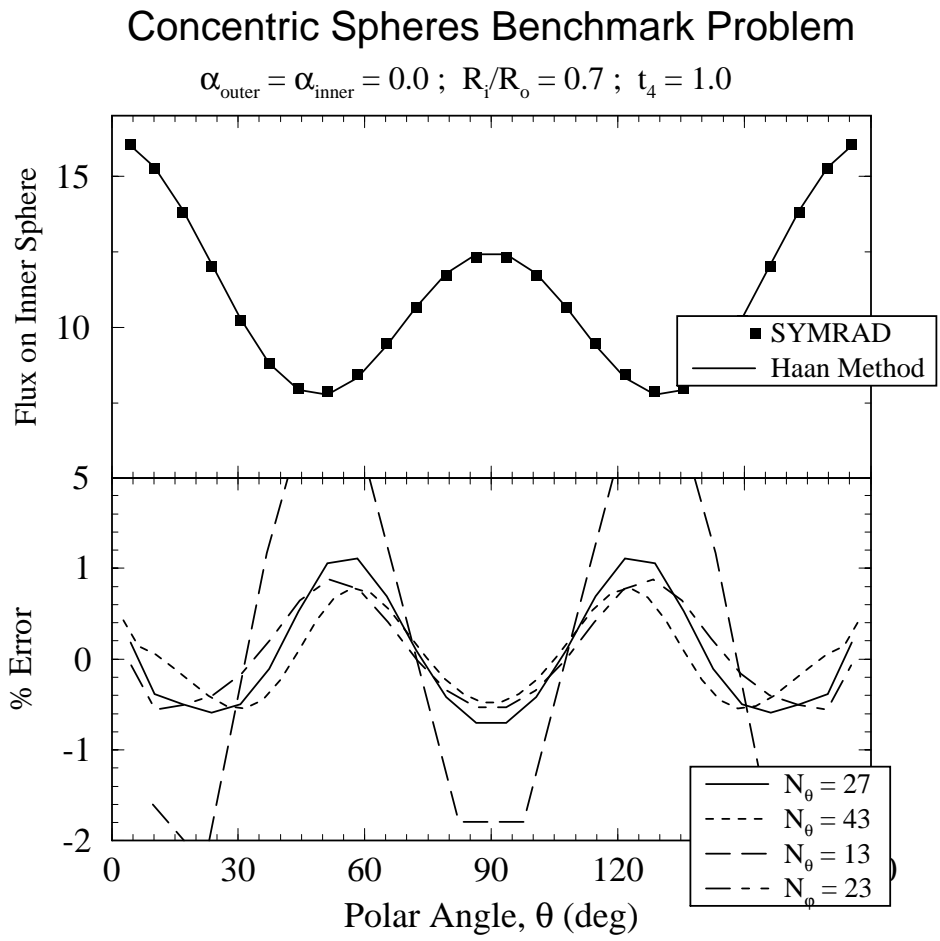


Figure 9.7. Comparison of incident flux distributions on inner sphere calculated using SYMRAD and from Haan's method for a P_4 source distribution. Results showing the dependence on the number of surface elements is also shown.

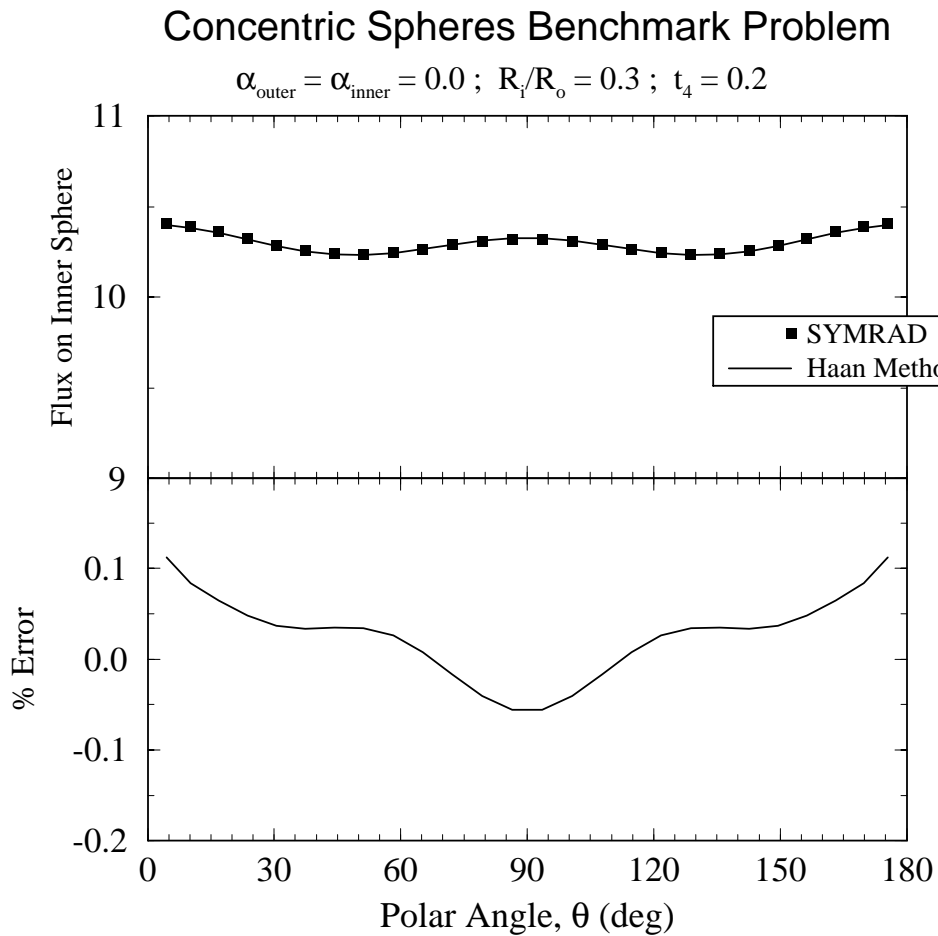


Figure 9.8. Comparison of incident flux distributions on inner sphere calculated using SYMRAD and from Haan's method for a P_4 source distribution.

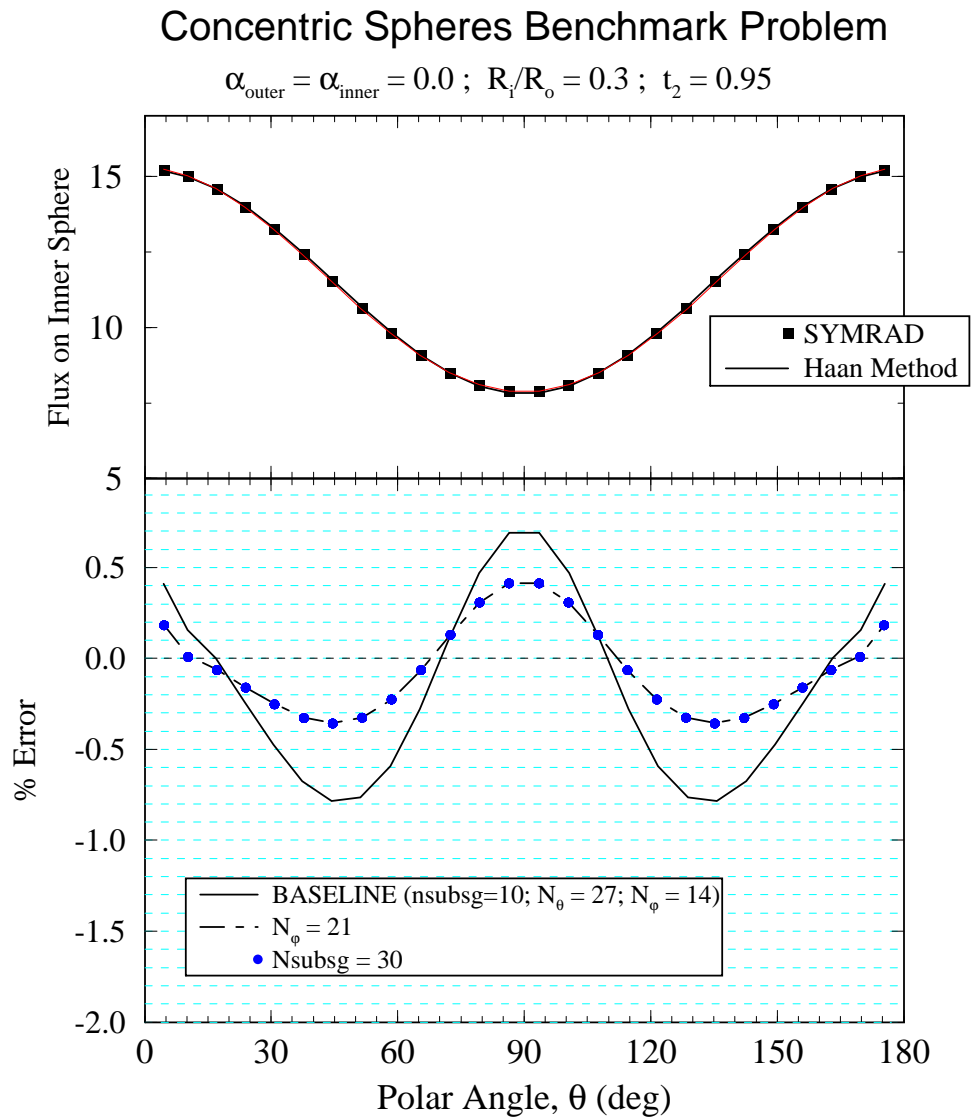


Figure 9.9. Comparison of incident flux distributions on inner sphere calculated using SYMRAD and from Haan's method for a P_2 source distribution.

In all cases, the differences between the SYMRAD and Haan results were $\lesssim 1\%$, so long as the number of azimuthal points was ≥ 14 and the number of polar points was ≥ 27 . The primary source of the errors stems from modeling the spheres as a finite number of polygons, while the errors arising from the configuration factor integration algorithms are relatively small.

9.3. Summary of Benchmark Simulations

The results presented in this section indicate that SYMRAD provides accurate solutions both to surface element-to-surface element configuration factor integrals and to concentric sphere flux asymmetry problems. In cases where analytic or “accurate numerical solutions” were available, SYMRAD was found to be in very good agreement. In addition, by comparing several different configuration factor integration techniques, we have been able to demonstrate that the algorithms used in SYMRAD are both accurate and computationally efficient.

10. Simulations of NOVA and OMEGA Radiation Symmetry Experiments

10.1. Simulation of NOVA Radiation Symmetry Experiments

To assess SYMRAD’s ability to simulate radiation asymmetries in ICF experiments, we performed simulations of cylindrical hohlraums with parameters relevant to experiments described in Suter et al. [18] and Hauer et al. [19]. In these experiments, implosion symmetry was studied through the use of imploded core images. The dependence of the distortion in the imploded core images was studied as a function of the cylindrical hohlraum length. Figure 10.1 (top) shows an illustration of the experimental geometry. As the hohlraum length increases the points at which the laser beams hit the hohlraum move further from the cylinder midplane, and the ratio of incident radiation on the capsule equator to that of the poles decreases. This leads to a greater distortion (see Figure 10.1 (bottom)), or “pancaking”, of the imploded core. Note that the data point with best symmetry in Figure 10.1 corresponds to a cylinder length of $2400 \mu\text{m}$ (or “pointing” = $L/2 = 1200 \mu\text{m}$). This value corresponds to experiments using pulse shape 22 (ps22). In a series of experiments using 1 ns flattop laser pulses, the best symmetry occurred for $L/2 = 1320 \pm 50 \mu\text{m}$ [18]. The differences have been attributed, at least in part, to spot motion (i.e., the movement of positions at which laser energy is deposited due to wall blowoff).

To simulate these experiments, we performed a series of time-independent SYMRAD calculations with the following parameters:

- $R_{capsule} = 275 \mu\text{m}$
- $R_{hohlraum} = 800 \mu\text{m}$
- $R_{LEH} = 600 \mu\text{m}$
- $\alpha_{hohlraum} = 0.8$
- $\alpha_{capsule} = 0.1$
- $2000 \mu\text{m} \leq L_{hohlraum} \leq 3000 \mu\text{m}$.

In each calculation, a total of 980 surface elements were used. The location of each laser spot on the cylinder wall was determined by the vector from the laser port in the target chamber to the center of the LEH through which the beam passes. The size of the laser spot on the wall is governed by the opening angle of the conical laser beam, which was assumed to be 10 degrees.

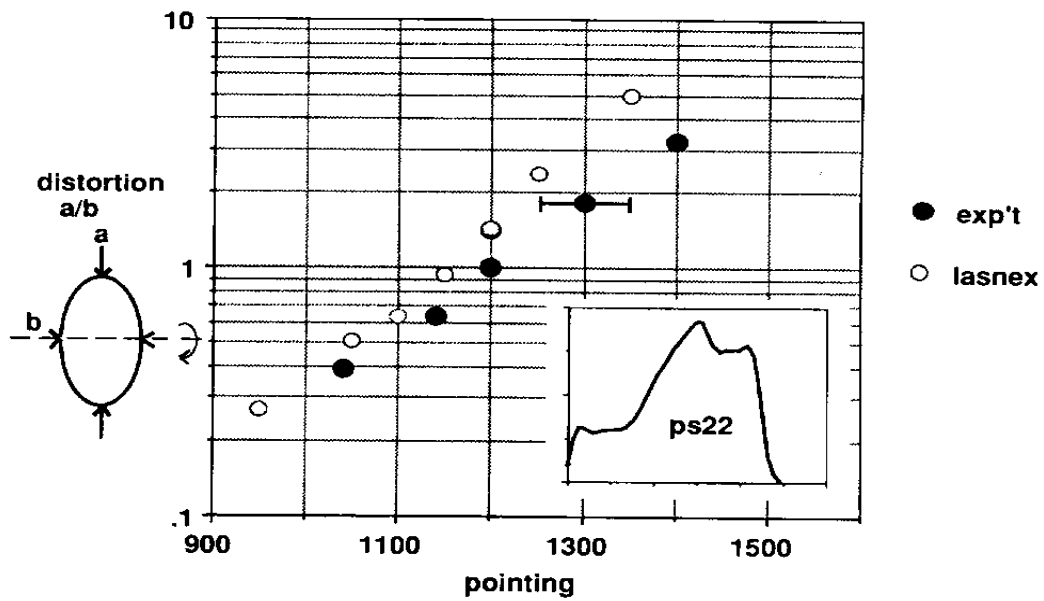
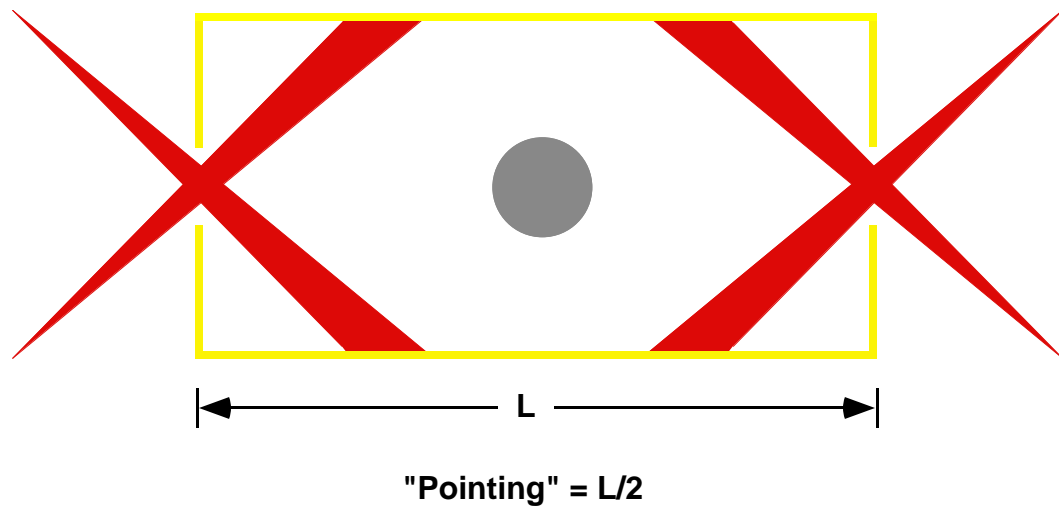


Figure 10.1. (Top) Illustration of experimental geometry in NOVA radiation symmetry experiments. (Bottom) Experimentally measured distortion as a function of "pointing", or $L/2$ (from Suter et al. [18]).

Figure 10.2 shows results for the calculated distribution of incident flux onto the capsule as a function of polar angle ($\theta = 0^\circ$ and 180° correspond to points below the LEH). The lower plot in Figure 10.2 displays the same results, but as the percent deviation from the mean flux onto the capsule. At each polar angle, there is a distribution of points (as opposed to a single point). This occurs because there is also an azimuthal dependence for the flux onto the capsule.

These time-independent SYMRAD simulations predict that the best symmetry occurs when the hohlraum half-length is $L/2 \approx 1300 \mu\text{m}$. This is consistent with the experimentally determined values of $1200 \pm 50 \mu\text{m}$ for a ps22 pulse and $1320 \pm 50 \mu\text{m}$ for a 1 ns flat-top pulse. Thus, the SYMRAD predictions appear to be in very good agreement with NOVA experimental symmetry data.

10.2. Simulation of OMEGA Tetrahedral Hohlräume

A series of calculations were also performed for tetrahedral hohlraums using parameters relevant to experiments which took place at the University of Rochester OMEGA facility in 1997. In these simulations, the energy source term was modeled by assuming the inside surface of the tetrahedral hohlraum — a sphere with 4 LEH located at angles corresponding to a tetrahedron — was uniform (*i.e.*, E_i in Eq. (6.1) was the same for all hohlraum surface elements). The nominal parameters in these simulations were:

- $R_{\text{hohlraum}} = 1150 \mu\text{m}$
- $R_{\text{LEH}} = 450 \mu\text{m}$
- $R_{\text{capsule}} = 275 \mu\text{m}$
- $\alpha_{\text{hohlraum}} = 0.8$
- $\alpha_{\text{capsule}} = 0.1$.

The radii were varied to study the sensitivity of the radiation asymmetry on the capsule to R_{LEH} , R_{cap} , and R_H . A total of 1200 surface elements was used in each calculation.

Figure 10.3 shows plots of the deviation from the mean incident radiation field on the capsule as a function of polar angle and azimuthal angle. In all cases, the color scale is the same. The top plot corresponds to results using LEH radii of $450 \mu\text{m}$. In this case, deviations exceeding $\pm 5\%$ are seen. The regions of purple indicate relatively low incident fluxes and correspond to points on the capsule which lie below each of the LEH. The lower two images in Figure 10.3 show that as the LEH radii decrease, the

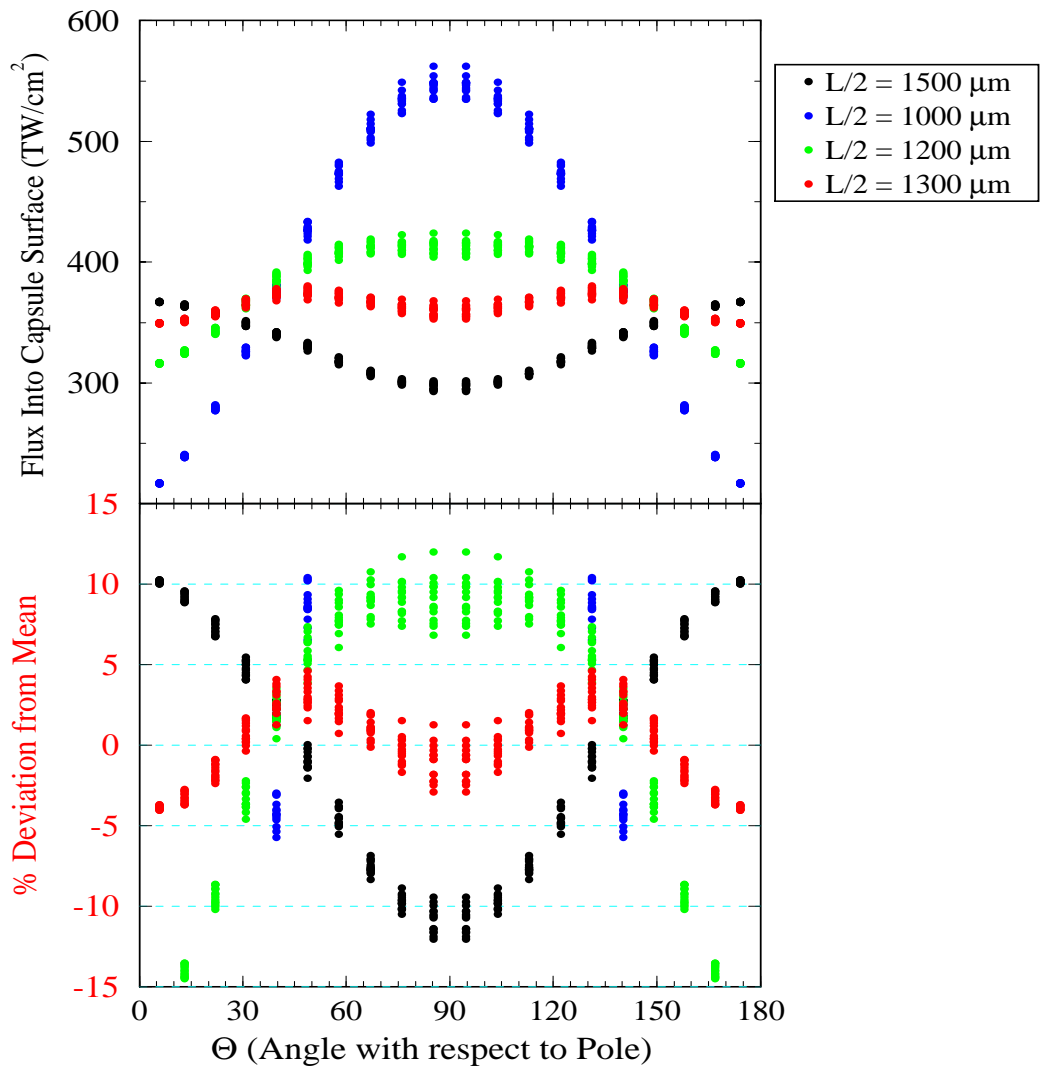


Figure 10.2. Calculated distributions of incident flux onto the capsule for parameters relevant to NOVA radiation symmetry experiments. The data in the bottom plot are the same as the top, but presented as the percent deviation from the mean incident flux.

uniformity of flux onto the capsule improves. For the case in which the LEH radii is 250 μm , the peak deviations from the mean incident flux are approximately $\pm 3\%$. For the case when $R_{LEH} = 50 \mu\text{m}$, the peak deviation is less than 1%.

Figure 10.4 shows three series of calculations in which the LEH radii were varied (top), the hohlraum radius was varied (middle), and the capsule radius was varied (bottom). The results show, as expected, that the RMS variation decreases as the case-to-capsule ratio increases. For the nominal parameters of $R_{LEH} = 450 \mu\text{m}$, $R_{cap} = 275 \mu\text{m}$, and $R_H = 1150 \mu\text{m}$, the RMS variation in the incident flux on the capsule is between 5 and 6 percent. Increasing the hohlraum radius to 1400 μm results in a drop in the RMS variation to about 3 percent.

Figure 10.5 shows the azimuthal dependence of the incident flux on the capsule for points located along the capsule “equator;” that is, as viewed looking down one of the LEH in the tetrahedral hohlraum. Results are shown for hohlraum radii of 900, 1150, and 1400 μm . The three valleys correspond to points on the capsule which lie approximately below one of the three remaining LEH. For $R_{LEH} = 900 \mu\text{m}$, the variation of incident flux about the equatorial belt is about $\pm 13\%$, while for $R_{LEH} = 1150 \mu\text{m}$, the variation is approximately $\pm 6\%$.

The above simulations represent a first step in the analysis of radiation symmetry data from OMEGA tetrahedral hohlraum experiments. It is anticipated that future simulations will include the actual laser beam pointings, as well as time-dependent laser powers and albedos.

Acknowledgment

Support for this work has been provided by the Los Alamos National Laboratory.

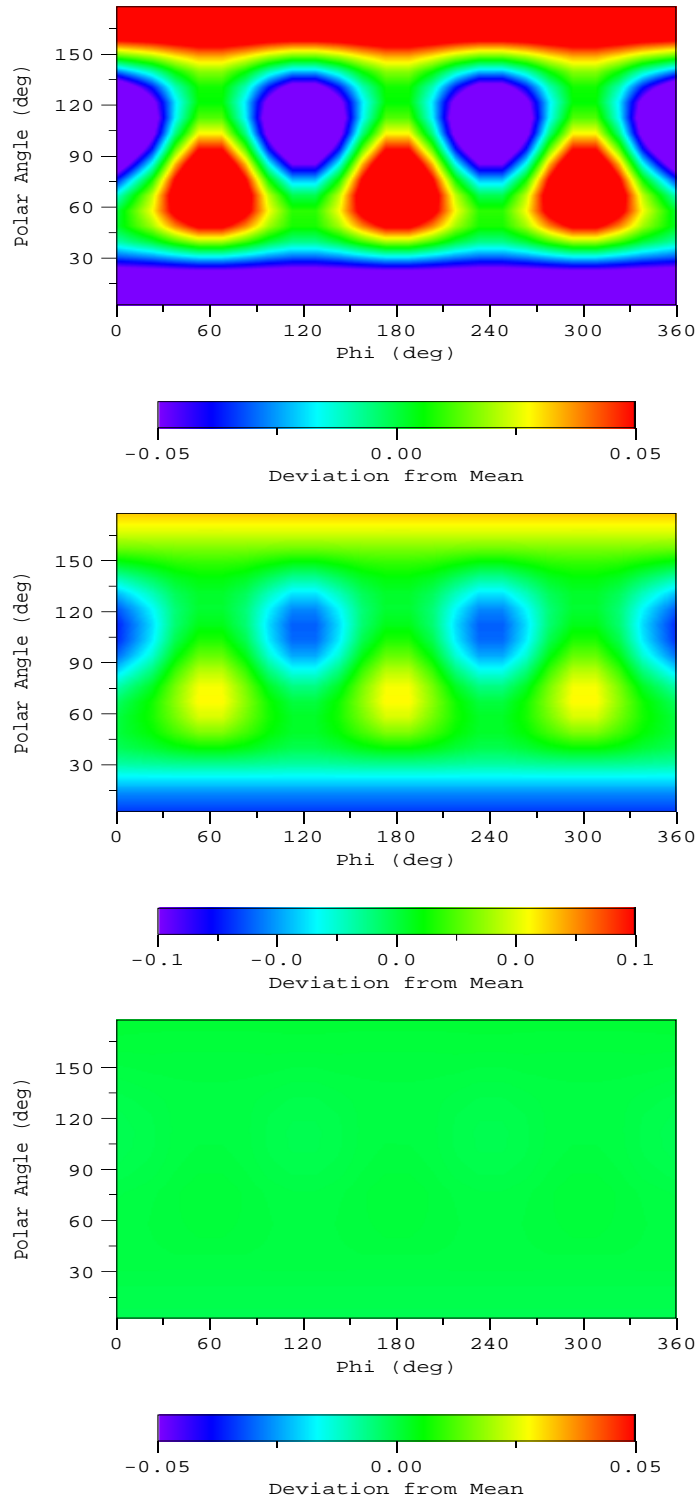


Figure 10.3. Images showing the dependence of the incident radiation flux onto a capsule in tetrahedral hohlraum targets as a function of the radii of the LEH: (top) $R_{LEH} = 450 \mu\text{m}$, (middle) $R_{LEH} = 250 \mu\text{m}$, (bottom) $R_{LEH} = 50 \mu\text{m}$. The images show the fractional deviation from the mean incident flux as a function of azimuthal angle (“Phi”) and polar angle. In each case, $R_{hohlraum} = 1150 \mu\text{m}$ and $R_{capsule} = 275 \mu\text{m}$.

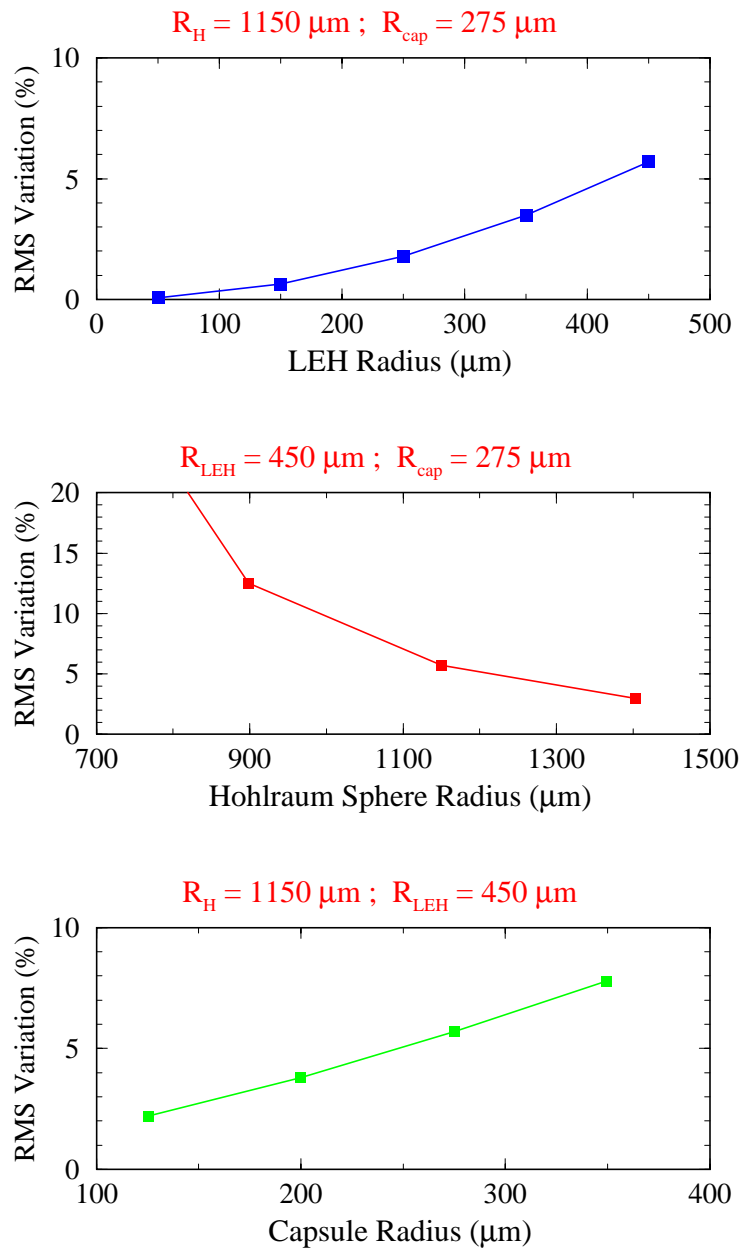


Figure 10.4. Dependence of RMS variation of incident flux onto the capsule as a function of LEH radii (top), hohlraum radius (middle), and capsule radius (bottom).

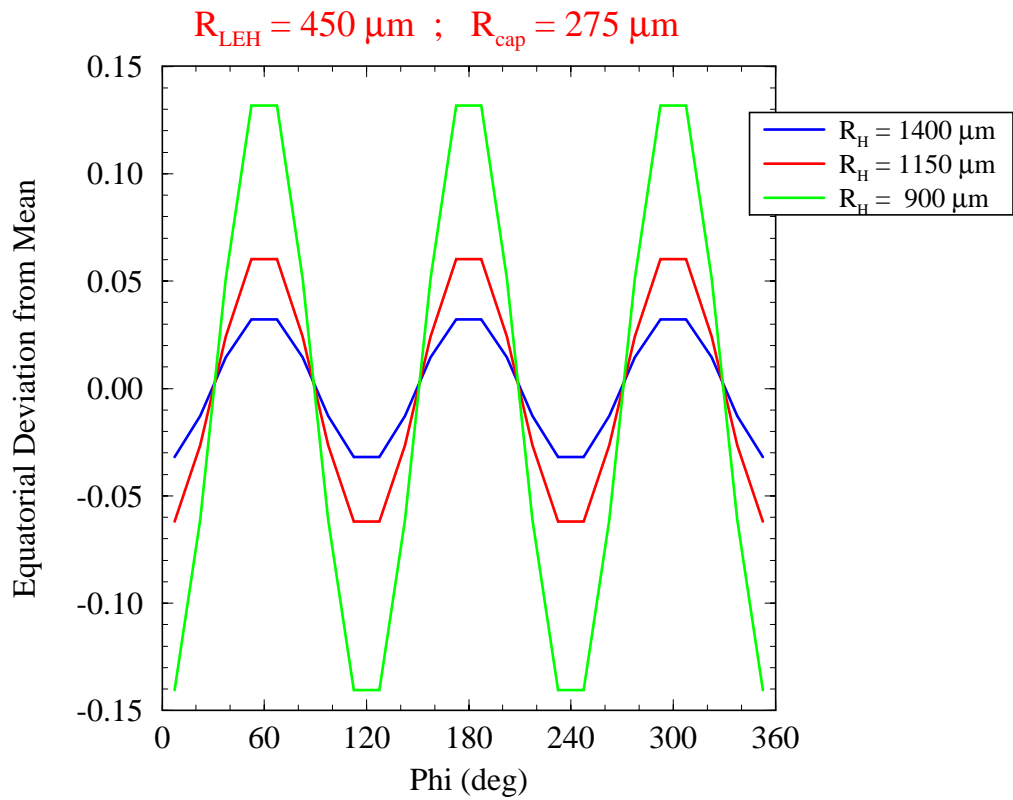


Figure 10.5. Calculated deviation from the mean incident flux onto the capsule “equator” as a function of azimuthal angle for tetrahedral hohlraum targets.

References

1. J. J. MacFarlane, G. A. Moses, and R. R. Peterson, “*BUCKY-1 – A 1-D Radiation-Hydrodynamics Code for Simulating Inertial Confinement Fusion High Energy Density Plasmas*,” University of Wisconsin Fusion Technology Institute Report UWFD-984 (August 1995).
2. Wang, P., “*EOSOPA – A Code for Computing the Equations of State and Opacities of High Temperature Plasmas with Detailed Atomic Models*,” University of Wisconsin Fusion Technology Institute Report UWFD-933 (December 1993).
3. Wang, P., MacFarlane, J. J., and Orzechowski, T. J., *Rev. Sci. Instrum.* **68**, 1107 (1997).
4. Goral, C. M., Torrance, K. E., Greenberg, D. P., and Battaile, B., *Computer Graphics (SIGGRAPH '84 Proceedings)* **18**, No. 3, 213, 1984.
5. Cohen, M. F., and Greenberg, D. P., *Computer Graphics (SIGGRAPH '84 Proceedings)* **19**, No. 3, 31, 1985.
6. Cohen, M. F., Chen, E., Wallace, J. R., and Greenberg, D. P., *Computer Graphics (SIGGRAPH '88 Proceedings)* **22**, No. 4, 75, 1988.
7. Wallace, J. R., Elmquist, K. A., and Haines, E. A., *Computer Graphics (SIGGRAPH '89 Proceedings)* **23**, No. 3, 315, 1989.
8. Baum, D. R., Rushmeier, H. E., and Winget, J. M., *Computer Graphics (SIGGRAPH '89 Proceedings)* **23**, No. 3, 325, 1989.
9. Drake, D. J., *J. Comp. Physics*, 1997.
10. Siegel, R., and Howell, J. R., *Thermal Radiation Heat Transfer, Third Edition*, Hemisphere Publishing, Washington DC, 1992.
11. Ashdown, I., *Radiosity, A Programmer's Perspective*, Wiley, New York, 1994.
12. Anderson, E., et al., *LAPACK Users' Guide*, SIAM, Philadelphia, 1992.
13. Woo, M., Neider, J., and Davis, T., *OpenGL Programming Guide*, Addison-Wesley, 1992.
14. Paul, B., “The MESA 3-D Graphics Library”, developed at the U. Wisconsin Space Science and Engineering Center, 1993-1996.
15. Magelssen, G. R., private communication, 1997.

16. Cooper, A. J., Kirkpatrick, R. C., Lindman, E. L., and Tabor, J. E., “*SNAP — A View Factor Code for Complex Geometries*,” Los Alamos National Laboratory Report LA-UR-86-1038 (1986).
17. Haan, S., “*Radiation Transport Between Concentric Spheres*,” Lawrence Livermore National Laboratory Report UCRL-ID-118152 (August 1994).
18. Suter, L. J., et al., *Phys. Rev. Letters* **73**, 2328 (1994).
19. Hauer, A. A., et al., *Rev. Sci. Instr.* **66**, 672 (1995).